Impacts of aerosol-radiation interaction on meteorological forecast over northern China by offline coupling the WRF-Chem simulated AOD into WRF: a case study during a heavy pollution event

Yang Yang[1], Min Chen[1], Xiujuan Zhao[1*], Dan Chen[1*], Shuiyong Fan[1], Jianping Guo[2], and Shaukat Ali[3]

1 Institute of Urban Meteorology, China Meteorological Administration, Beijing 100089, China

2 State Key Laboratory of Severe Weather, Chinese Academy of Meteorological Sciences, Beijing, 100081, China

3 Global Change Impact Studies Centre, Ministry of Climate Change, Islamabad 44000, Pakistan

Abstract

To facilitate the future inclusion of aerosol-radiation interactions in the regional operational Numerical Weather Prediction (NWP) system – RMAPS-ST (adapted from Weather Research and Forecasting, WRF) at the Institute of Urban Meteorology (IUM), China Meteorological Administration (CMA), the impacts of aerosol-radiation interactions on the forecast of surface radiation and meteorological parameters during a heavy pollution event (December 6^{th} -10^{th}, 2015) over northern China were investigated. The aerosol information was simulated by RMAPS-Chem (adapted from WRF model coupled with Chemistry, WRF-Chem) and then offline-coupled into Rapid Radiative Transfer Model for General Circulation Models (RRTMG) radiation scheme of WRF to enable the aerosol-radiation feedback in the forecast. To ensure the accuracy of high-frequency (hourly) updated aerosol optical depth (AOD) field, the temporal and spatial variations of simulated AOD and aerosol extinction coefficient at 550nm were evaluated against in-situ and satellite observations. Comparisons with in-situ and Moderate Resolution Imaging Spectroradiometer (MODIS), AErosol Robotic NETwork (AERONET), and Cloud-Aerosol Lidar and Infrared Pathfinder Satellite Observation (CALIPSO) satellite observations showed that the model could reproduce and spatial and vertical distribution as well as the temporal variation the of polluted episode. Further comparison of $PM_{2.5}$ with in-situ observation showed WRF-Chem reasonably captured the $PM_{2.5}$ field in terms of spatial distribution and magnitude, with the

correlation coefficients of 0.85, 0.89, 0.76, 0.92 and 0.77 at Beijing, Shijiazhuang, Tianjin, Hebei and Henan, respectively. Forecasts with/without the aerosol information were conducted further, and the differences of surface radiation, energy budget, and meteorological parameters were evaluated against surface and sounding observations. The offline-coupling simulation (with aerosol-radiation interaction active) showed a remarkable decrease of downward shortwave (SW) radiation reaching surface, thus helping to reduce the overestimated SW radiation during daytime. The simulated surface radiation budget was also improved, with the biases of net surface radiation decreased by 85.3%, 50.0%, 35.4%, and 44.1% during daytime at Beijing, Tianjin, Taiyuan and Jinan respectively, accompanied by the reduction of sensible (16.1 W m^{-2}, 18.5%) and latent (6.8 W m^{-2}, 13.4%) heat fluxes emitted by the surface at noon-time. In addition, the cooling of 2-m temperature (~0.40 °C) and the decrease of horizontal wind speed near surface (~0.08 m s^{-1}) caused by the aerosol-radiation interaction over northern China helped to reduce the bias by ~73.9% and ~7.8% respectively, particularly during daytime. Further comparisons indicated that the simulation implemented AOD could better capture the vertical structure of atmospheric wind. Accompanied with the lower planetary boundary layer and the increased atmospheric stability, both U and V wind at 850hPa showed the convergence which were unfavorable for pollutants dispersion. Since RMPAS-ST provides meteorological initial condition for RMAPS-Chem, the changes of meteorology introduced by aerosol-radiation interaction would routinely

impact the simulations of pollutants. To verify the statistically significance of the results, we further conducted the 24-hour forecasts for a longer period lasting 27 days (Jan. 13th – Feb. 8th, 2017), with no AOD field (NoAero) and WRF-Chem simulated hourly AOD fields (Aero) included, as well as constant AOD value of 0.12 (ClimAero), respectively. The one-month results were statistically significant and indicated that the mean RMSE of 2-m temperature (wind speed at 10m) in Aero and ClimAero relative to NoAero was reduced by 3.95% (1.86%) and 1.23% (1.63%). More detailed evaluations and analysis will be addressed in a future article. These results demonstrated the profound influence of aerosol-radiation interactions on the improvement of predictive accuracy and the potential prospects to offline couple near-real-time aerosol information in regional RMAPS-ST NWP in northern China.

Key words: Aerosol-radiation interactions, offline-coupling, WRF, northern China, pollution

1. Introduction

Aerosol-radiation interactions modify the radiative energy budget of the earth-atmosphere system through the interaction between aerosols and solar radiation by scattering and absorbing mechanism as well as the absorption and emitting of thermal radiation (Ramanathan et al., 2001; Yu et al., 2006). The aerosol-radiation interaction may cool or heat the earth-atmosphere system, alter surface and atmospheric radiation and temperature structure on regional and global climate, which have been widely reported and studied (Hansen et al., 1997; Ramanathan et al., 2001; Kaufman et al., 2002; Liao et al., 2006; Zhang et al., 2010; Ghan et al., 2012; Yang et al., 2017a). Considering the lifetime of most aerosol particles and their locally uneven distribution, as well as their high dependence on emission sources and local meteorological conditions for dispersion (Rodwell and Jung, 2008; Liu et al., 2012; Liao et al, 2015), the impacts of episodic aerosol events over regional areas are worthy of more concerns (Cheng et al., 2017; Zheng et al., 2019).

With substantial aerosol loading, aerosol particles have significant influences on meteorology, and many endeavors by both field experiments and numerical models have been devoted to study the impacts of aerosol-radiation interaction on meteorological fields, including surface solar radiation, planetary boundary layer (PBL), atmospheric heating rate, atmospheric stability (Hansen et al., 1997; Ackerman et al., 2000; Quan et al., 2014; Yang et al., 2017b; Wang et al., 2018), cloud formation due to thermodynamic changes, and further the onset or reduction of precipitation

systems (Grell et al., 2011; Guo et al., 2016, Jiang et al., 2017). For instance, in worldwide, the simulations with Weather Research and Forecasting (WRF) model coupled with Chemistry (WRF-Chem) showed that by purely taking into account the aerosol-radiation interactions, aerosols may reduce incoming solar radiation by up to −9% (−16%) and 2-m temperatures by up to 0.16°C (0.37°C) in January (July) over the continental U.S. (Zhang et al., 2010) , affect meso-scale convection system owing to thermodynamic changes over Atlantic Ocean during Saharan dust eruption period (Chen et al., 2017), and lead to the distinct changes in precipitation due to the changes in temperature profile and stabilities induced by the aerosol-radiation interaction over Eastern China (Huang et al., 2016).

Northern China is experiencing heavy air pollution in past two decades, with particle matter (PM) being the primary pollutant, particularly during wintertime (Chan and Yao, 2008; Zhang et al., 2015; Zhao et al., 2019) due to the combination of high primary and precursor emissions and frequent stable meteorological conditions in this area (Elser et al., 2016; Zhang et al, 2018). The effects of aerosol-radiation interaction on meteorology were expected to be much more significant over northern China. Applying WRF and Community Multi-scale Air Quality Model (CMAQ) system (WRF-CMAQ), Wang et al. (2014) and Sekiguchi et al. (2018) reported a 53% reduction in solar radiation reaching surface and ~100m decrease of planetary boundary layer height (PBLH) in response to the presence of aerosols during a severe winter haze episode in China. Wang et al. (2015a, b) used the online chemical weather

111 forecasting mode Global/Regional Assimilation and PrEdiction System/ Chinese
112 Unified Atmospheric Chemistry Environment (GRAPES/CUACE) and illustrated that
113 the solar radiation at ground decreased by 15% in Beijing–TianJin–Hebei, China, and
114 its near surroundings, accompanied by the decrease in turbulence diffusion of about
115 52% and a decrease in PBLH of about 33 % during a haze episode of summertime in
116 2008.

117 Considering the significant influence of the aerosol-radiation interaction on
118 meteorological forecasts as illustrated in many studies (Kaufman et al., 2002; Zhang
119 et al., 2010), several weather forecast centers are conducting research to facilitate the
120 inclusion of more complex aerosol information in operational numerical weather
121 prediction (NWP) models. For example, Rodwell and Jung (2008) showed the local
122 medium-range forecast skills were improved due to the application of new
123 climatological aerosol distribution in European Centre for Medium-Range Weather
124 Forecasts (ECMWF). Recently, a positive impact up to a 48h lead time on the 2m
125 temperature and forecasts of surface radiative fluxes were reported in ECMWF by
126 applying the prognostic aerosols compared to the monthly climatological aerosol
127 (Rémy et al., 2015). Toll et al. (2016) found that the inclusion of aerosol effects in
128 NWP system was beneficial to the accuracy of simulated radiative fluxes, temperature
129 and humidity in the lower troposphere over Europe. In addition, it was shown that the
130 quality of weather forecasts at UK MET office can be further advanced when the
131 real-time aerosol distribution rather than climatological distribution was included,

with the decreased bias of downward SW at surface (−2.79 W m^{-2} vs. −5.30 W m^{-2}) and the mean sea-level pressure (0.71hPa vs. 0.80hPa) (Mulcahy et al., 2014; Toll et al., 2015). For these research serving for operational NWP systems, both online and offline approaches (that aerosol information were simulated by separate chemistry system and then offline coupled to NWP model) were widely used.

In most previous research-targeted modeling studies over northern China, the aerosol-radiation interaction has been widely assessedin online-coupled meteorology-chemistry models, which might not be practical for NWP purpose. Considering aerosol particles differ by morphology, size and chemical composition, therefore, the numerical treatment of aerosol particles in atmospheric models needs sophisticated method and considerable simplifications, which may bring in more assumptions and uncertainties in online coupling (Baklanov et al., 2014). Moreover, the online simulations require quite high computational costs and could not meet the requirement of efficiency for operational NWP. Grell and Baklanov (2011) illustrated that the offline approach could generate to almost identical results compared to online simulation with the offline-coupling intervals about 0.5-1h. Thus, the computational-economic offline simulation provides a feasible and computationally less demanding approach to include the aerosol-radiation interaction in an operational NWP system. Péré et al. (2011) adopted an offline-coupling between the chemistry-transport model CHIMERE and WRF to study the radiative forcing of high load aerosols during the heat wave of summer in 2003 over Western Europe. Wang et

al. (2018) offline implemented the daily AOD from Moderate Resolution Imaging Spectroradiometer (MODIS) to WRF during a heavy winter pollution at Beijing to study the effect of aerosols on boundary layer. Still, there have been few studies that adopted offline simulation to investigate the impacts of aerosol-radiation interactions over northern China in an NWP system. At Institute of Urban Meteorology, regional operational NWP system–RMAPS-ST (adapted from WRF) and regional air quality model–RMPSA-Chem (adapted from WRF-Chem) were applied operationally. In this study, we investigate the radiative effects of aerosols and their feedbacks on weather forecasting over northern China during a polluted event occurred in winter of 2015, and further potential impacts of changed meteorology to the transport and dissipation of pollution. The simulations were in the configurations of the two systems, aiming at presenting the offline-coupling of the high-frequent real-time aerosol distribution simulated by WRF-Chem and WRF, and evaluating the potential effects of aerosol-radiation interactions on the forecast skills in the RMAPS-ST system for future applications.

The remainder of the paper is organized as follows. Section 2 presents the model configuration and experimental design. In section 3, the model's capabilities in capturing and forecasting the pollution episode are validated with observations first, and impacts of aerosol-radiation interactions on meteorological forecasting over northern China are analyzed further. The final section provides the concluding remarks.

2. Model description and experimental design

WRF is a state-of-the-art atmospheric modeling system designed for both meteorological research and NWP. The WRF version 3.8.1 released in August, 2016 was used in this study for a domain covering the northern China with a horizontal resolulation of 9km (222×201 grid points, Fig. 1a), and for 50 vertical levels. The lateral boundary condications (BCs) and initial conditions (ICs) for meteorological variables are provided by the forecast of ECMWF. The major physical schemes include the Assymetric Convective Model Version 2 (ACM2) PBL scheme (Pleim, 2007), the Thompson microphysics without aerosol-aware option (Thompson et al., 2008), the Kain-Fritsch cumulus parameterization (Kain, 2004), and the National Center for Environmental Prediction, Oregon State University, Air Force, and Hydrologic Research Lab's (NOAH) land-surface module (Chen and Dudhia, 2001; Ek et al., 2003). The landuse data have been reprocessed, with a higher accuracy and finer classification for urban areas (Zhang et al., 2013) and the urban canopy model (UCM) was not actived.

The shortwave and longwave radiation scheme is the Rapid Radiative Transfer Model for General Circulation Models (RRTMG) (Iacono et al., 2008). The RRTMG scheme is a new version of RRTM added in Version 3.1, and includes the Monte Carlo Independent Column Approximation (MCICA) method of random cloud overlap. A recent intercomparison study showed that the RRTMG had relativlely smaller mean errors in solar flux at the surface and the top of the atmosphere

(Oreopoulos et al., 2012) and was considered as recommended WRF configuration for air quality modeling (Rogers et al., 2013). The RRTMG scheme is capable to include the climatological aerosol data with spatial and temporal variations or an external time varing 3D aerosol input through the option of AER_OPT (Ruiz-Arias et al., 2014). In the present study, the real-time hourly aerosol optical depth (AOD) at 550nm from external files was input into WRF following the second approach. The AOD at 550nm was calculated as the vertical integral of extinction coefficients at 550nm from WRF-Chem simulation.

WRF-Chem version 3.3.1 was applied in this study, and the horizontal resolution was 9 km, with 222×201 grid points covering northern China, which was the same configurion of WRF mentioned above. WRF-Chem simulates the formation, transformation and transport processes of both primary and secondary atmospheric pollutants, including gases and PM species (Zhao et al., 2019). Physical parameterizations included single-layer Urban Canopy Model, Noah land-surface, Yonsei University (YSU) PBL, Grell-Devenyi ensemble convection, Thompson microphysics, and RRTM longwave and Goddard shortwave radiation (Chen and Dudhia, 2001; Hong et al., 2006; Grell and Dévényi, 2002; Thompson et al., 2008; Mlawer et al., 1997; Chou and Suarez, 1999). Carbon bond mechanism Z (CBMZ) including comprehensive reactions and alterable scenarios were used as the gas-phase mechanism. Model for Simulating Aerosol Interactions and Chemistry (MOSAIC) are used with four size bins (Zaveri and Peters, 1999). Anthropogenic

emission data were from the MEIC (2012) inventory (http://www.meicmodel.org/) with a resolution of 0.1 °×0.1 °. Meteorological ICs and BCs were obtained from the Final Analysis data (FNL) with a resolution of 1.0 °×1.0 ° from the National Centers for Environmental Prediction (NCEP). To generate aerosol fields for study period (Dec. 2^{nd}-11^{th}), 9-days WRF-Chem simulations from Dec. 2^{nd} were conducted using prescribed idealized profiles as ICs and BCs for chemical species.

To estimate the aerosol radiative forcing and its feedbacks on meteorological fields, two sets of 24-hour WRF forecasts were conducted at 00UTC from 2^{nd}-10^{th} December 2015. The only difference between the two sets of forecasts is whether the aerosol radiative feedback is activated (Aero, with WRF-Chem simulated hourly AOD fields as input fields) or not (NoAero, no aerosol included), and other schemes remained the same. It is noted that the aerosol-cloud interactions were not included in the study.

The sites of observations over simulated domain and northern China plain (NCP, purple box in Fig. 1a) were shown in Fig. 1. The 550nm AOD retrievals from Level 2 of MODIS sensors onboard polar orbiting satellites Terra and Aqua satellites were adopted to evaluate the spatial distribution of modeled AOD. The vertical distribution of aerosol extinction coefficient at 550nm were compared with that from Cloud-Aerosol Lidar and Infrared Pathfinder Satellite Observations (CALIPSO) satellite. Moreover, three sites of AErosol Robotic NETwork (AERONET) were used to validate the simulation (black dots in Fig. 1b), and the observed AOD

obtained from observation at the Institute of Atmospheric Physics (IAP), Chinese Academy of Sciences (39°58′ 28″ N, 116°22′ 16″ E) in Beijing city (blue dot in Fig. 1b) was also included as supplementary. The hourly observed $PM_{2.5}$ concentrations of total 813/332 monitoring stations over the study domain/NCP were from the released data by the China National Environmental Monitoring Centre (http://106.37.208.233:20035/, colored dots in Fig. 3a). For given cities (dots in Fig. 1a), hourly $PM_{2.5}$ concentration was represented by the average of data from all monitoring sites located in the city. Simulated meteorological variables including 2-m temperature and wind speed at 10m were evaluated using in-situ observations from National Meteorological Information Center (http://data.cma.cn/data/cdcindex.html) of China Meteorological Administration (CMA, dots in Fig. 8a). The radiations were observed at IAP and in-situ stations of CMA (shown as triangles in Fig. 1a). The vertical observation of atmospheric wind speed from sounding were also used (circles in Fig. 1a). The variables, sources, numbers of sites in the domain and NCP and the frequency of chemical and meteorological observations were also listed in Table 1.

3. Results

3.1 Evaluation of AOD and $PM_{2.5}$ simulated by WRF-Chem

Before the offline-coupling of the WRF-Chem simulated hourly AOD to meteorological model WRF, we first validated the simulated AOD and ensured the model's capability to reproduce the features of the aerosol field. Figure 2 shows the

spatial distribution of modeled AOD and AOD from MODIS Terra and Aqua. It was seen that WRF-Chem is capable to capture the AOD spatial distribution and also reproduced the transport paths during the event. The simulated high-valued AOD located in Henan on Dec. 6th, then the center moved to Hebei and Beijing on 7th and shifted to northeast areas afterwards. The variations of simulated AOD were in consistent with both Terra and Aqua with slightly overestimated peak value of AOD. In particular, the simulated shifting of AOD center to northeast areas was also observed in Aqua (Fig. 2r-s). To further verify the vertical distribution of aerosol extinction coefficient, Fig. 3 displayed the vertical distribution of simulated 550nm aerosol extinction coefficient compared to those from CALIPSO. Four cross sections along CALIPSO paths on 6th to 9th December were shown. The results indicated that the model could generally reproduce the vertical distribution of extinction coefficients at 550nm in terms of comparable magnitude with those from CALIPSO, particularly on 6th, 7th and 9th, December. However, CALIPSO showed more high values at lower altitude (below 1km) that model failed to capture; the inconsistency may be associated with both CALIPSO retrieval uncertainties at the low altitude and the model itself. Figure 4 further displayed the temporal variation of simulated AOD at 550nm (blue solid) at four sites, in comparison with three AERONET stations (black circles in Figs. 4a-c) and IAP site (black circles in Fig. 4d) for the period during 3rd to 11th December, 2015 (local time, LT). As shown in blue solids in Fig. 4a, the simulated AOD increased since 6th Dec. and reached the peak value of 9 on

279 7^{th}, and the high AOD value maintained until 9^{th} and reached the second peak. The
280 second peak was also observed from AERONET though most of them were missing
281 during the pollution event. The temporal variations of AOD at Beijing-CMA and
282 IAP (Figs. 4b and d) were similar to those at Beijing station (Fig. 4a). Meanwhile,
283 the simulated AOD at Xianghe (Fig. 4c) was relatively lower than those at other
284 stations.

285 Considering that the aerosol extinction was mainly attributed to scattering and
286 absorption of solar radiation by $PM_{2.5}$ and their hygroscopic growth with relative
287 humidity (Cheng et al., 2006), next we compared the simulated $PM_{2.5}$ concentrations
288 with corresponding in-situ observation over the model domain. As shown in Fig. 5,
289 the simulated and observed pollution were both initiated over Henan province on 6^{th},
290 further intensified and shifted northward afterwards. The polluted center located
291 over south of Hebei province and maintained until 10^{th}, with the maximum $PM_{2.5}$
292 concentration exceeding 440μg m^{-3}. The results indicated that WRF-Chem could
293 well capture the spatial features of $PM_{2.5}$ and its temporal variation, in spite of the
294 slight discrepancy of the center position during 9^{th} and 10^{th}. Figure 6 displayed the
295 mean bias, root mean square error (RMSE), and correlation coefficient during the
296 heavy pollution and relatively cleaner periods. It was seen that the biases of $PM_{2.5}$
297 were generally less than 40 μg m^{-3} with the correlation coefficient exceeding 0.8
298 during clean period (Fig. 6a-c). Compared with clean period, the bias and RMSE
299 were generally larger during polluted period (Fig. 6d-f). The $PM_{2.5}$ concentrations

over most areas of the domain were underestimated with the maximum bias exceeding 160μg m^{-3}. Overall, the correlation coefficient was generally higher than 0.4 in northern China during the polluted period, particularly over Beijing with the correlation coefficient reaching 0.8.

To further assess the temporal evolutions of the pollution, the simulated $PM_{2.5}$ concentrations at three major cities (Beijing, Shijiazhuang and Tianjin, shown as black dots in Fig. 1a) and two provinces (Hebei and Henan) in northern China were compared with observation as shown in Fig. 7. It showed that the hourly variations of $PM_{2.5}$ concentration, including the occurrence of several high peaks at the three cities, as well as the gradual accumulation of pollution in Hebei and Henan could be reasonably reproduced by WRF-Chem. The correlation coefficients (R) between simulation and observation at Beijing, Shijiazhuang, Tianjin, Hebei and Henan were 0.85, 0.89, 0.76, 0.92 and 0.77 respectively. It should be noted that there exits slight overestimation (underestimation) of the peak magnitude during 9^{th} to 10^{th} at Beijing and Shijiazhuang (Tianjin, Hebei and Henan); the overestimation in Beijing and Shijiazhuang is possibly associated with the frequent emission changes caused by emission-control-measures in reality which are not dynamically updated in the model; the underestimation is more related with the deficiency of model skills, such as missing heterogeneous reaction paths in the chemistry scheme.

3.2 Aerosol effects on meteorological simulations

In this section, the influences of aerosol-radiation interaction on the spatial and

temporal variations of radiation and energy budget simulated by WRF model were analyzed, and their impacts on the forecasts of meteorological fields were discussed further.

3.2.1 Aerosol impacts on simulations of radiative forcing and heat fluxes

To illustrate the impacts of aerosol-radiation interaction on the forecasts of radiation during the pollution event, the simulated surface downward SW radiation and net radiation at Beijing, Tianjin, Taiyuan and Jinan, as denoted by the triangles in Fig. 1a, were compared with observations in Fig. 8. To show the relationship with aerosol, the time series of AOD for Dec. 3^{th} -11^{th} were overlaid as gray shadings in Fig. 8. During the clean stage with quite low AOD values (close to 0) before 6^{th} Dec., both simulations with and without aerosols reasonably reproduced the temporal variation of downward SW at Beijing despite the slightly overestimation during the noon-time (Fig. 8a). However, the overestimated downward SW in NoAero turned to intensify extensively since 6^{th} Dec. and sustained till 10^{th} Dec., accompanied by the occurrence of the pollution with the high AOD value. Meanwhile, the downward SW was much lower in Aero than that in NoAero due to aerosol extinction, with resembled temporal variations and comparable magnitude at the peak time compared to the observations. Similarly, the variations of downward SW from Aero simulation were also closer to observations at Tianjin, Taiyuan and Jinan than those in NoAero (Figs. 8b-d). It was noted that the most significant improvement of simulated downward SW at Jinan appeared on 10^{th} Dec. and was later than that at Beijing,

342 which was consistent with the AOD's variations at Jinan. Moreover, the surface
343 energy balance was also affected by the reduction of downward SW radiation
344 reaching the ground due to the presence of aerosol particles. As shown in Figs. 8e–h,
345 in corresponding to the changes in downward SW, the variations of net radiation at
346 surface in Aero were also in better agreement with observation during the polluted
347 period than in NoAero, particularly during daytime with the high AOD values.
348 To further quantify the influence of the aerosol-radiation interaction on the
349 diurnal variation of surface radiation, next we compared the simulated averaged
350 diurnal variation of downward SW and net radiation during the polluted episode (6^{th}
351 to 10^{th}) with observation. Figure 9a showed that there existed a large overestimation
352 of surface downward SW during the daytime in NoAero. Particularly, the
353 overestimated downward SW tented to increase since morning (0800 LT) and peak
354 at noon (1300 LT) with the maximum bias reaching 226.5 W m^{-2}, and the mean bias
355 of ~149.4 W m^{-2} during daytime (averaged during 0800 to 1800 LT, Table 2).
356 However, the overestimated SW radiation was remarkably reduced in Aero with the
357 mean bias of 38.0 W m^{-2} during daytime. Similarly, the diurnal variation and
358 magnitude of downward SW radiation at surface were also better captured at Tianjin,
359 Taiyuan and Jinan in Aero (Figs. 9b–d), with the lower bias (70.9 W m^{-2}, 118.3 W
360 m^{-2} and 97.7 W m^{-2}) than in NoAero (115.5 W m^{-2}, 155.0 W m^{-2} and 149.1 W m^{-2})
361 during daytime. Note the biases of SW radiation in Tianjin, Taiyuan and Jinan were
362 not improved as much as in Beijing due to the lower AOD. Consistent with this

finding, the reduction of downward SW was also reported in United States (Zhang et al., 2010) and Europe (Toll et al., 2016) with relatively lower decrease (10 W m^{-2} and 18 W m^{-2}); the relatively larger reductions (30-110 W m^{-2}) in northern China is possibly due to the higher aerosol load. Figures 9e–h presented the diurnal variations of net radiation, with positive (negative) net radiation during daytime (nighttime) in observation, and the NoAero tended to overestimate (underestimate) the net radiation at surface during daytime (nighttime), indicating that there existed surplus energy income and outcome in model than those in observation, inducing the larger magnitude of diurnal cycle of net radiation. By including the aerosol-radiation interaction in the model, the simulated diurnal variations of net radiation were markedly improved, particularly during daytime with the reduction of bias by 85.3%, 50.0%, 35.4%, and 44.1% at Beijing, Tianjin, Taiyuan and Jinan, respectively.

In response to the decrease of downward SW radiation and net radiation at the ground during daytime, the surface fluxes also changed in presence of aerosol extinction within the energy-balanced system. Figure 10 displayed the difference of surface sensible and latent heat flux between Aero and NoAero at 1300LT, when the influences of the aerosol on radiation reaching the peak. Comparing to the NoAero simulation, both the surface sensible and latent heat flux emitted by the surface were reduced in the Aero simulation, with the domain-average of 16.1 W m^{-2} (18.5%) and 6.8 W m^{-2} (13.4%) respectively. It was noted that the decrease of the surface latent heat flux was less pronounced than that of surface sensible heat flux, suggesting the

384 impact of aerosol-radiation interaction on the humidity was less significant than that
385 of temperature, which was also reported over United States (Fan et al., 2008) and
386 western Europe (Péré et al., 2011).

387 **3.2.2 Aerosol impacts on simulations of temperature, PBLH and wind fields**

388 The changes in radiation and energy budget through the impacts of
389 aerosol-radiation interaction would certainly induce the changes in PBL
390 thermodynamics and dynamics, which would result in changes in the forecasts of
391 meteorological fields. The impacts on the forecasts of 2-m temperature, PBLH and
392 wind fields due to the aerosol-radiation interaction are discussed in the following
393 subsection.

394 Figure 11 presented the diurnal variation of averaged bias of 2-m temperature
395 during polluted period in NoAero (upper panel) and Aero (lower panel) compared
396 with the in-situ observation during 1100 LT to 2300 LT. It was obvious that the
397 temperature of NoAero was significantly overestimated for a wide range over
398 northern China, particularly over the plain areas including south of Hebei, Henan
399 and Shanxi provinces. The warm biases tended to intensify in the afternoon and
400 reach ~3°C over south part of Hebei province (Figs. 11b–c). Accompanied by the
401 warm biased over plain areas throughout the day, the mountain areas were
402 dominated by the cold biases until 1700 LT, and turned to be warm biases afterwards,
403 which were attributed by the frozen water in soil due to wet bias of soil moisture
404 over mountain areas, inducing overestimated energy transport from atmosphere to

soil during daytime. Compared to NoAero, the lower temperature in Aero due to the decreased surface solar radiation, caused by aerosol extinction led to the reduced warm bias in NCP region. However, the cold bias in Beijing area was slightly intensified, which may partly relevant with the overestimated $PM_{2.5}$ concentration in Beijing and can be improved by incorporating more accurate aerosol information in the future. It was noted that the cold biases over mountain areas associated with the model physics deficiency can not be corrected by aerosol-radiation effects, thus the correction of aerosol-radiation effect may get complex results and differ with regions due to the model pre-existing deficiencies.

To quantitatively evaluate the agreement of simulated 2-m temperature with observations, the mean bias and RMSE were employed, and their averaged diurnal variations during the polluted episode (6^{th} to 10^{th}, Dec.) averaged over NCP, denoted by the purple box in Fig. 1a, were displayed in Fig. 12. As shown in Fig. 12a, the warm bias in NoAero sustained during the entire 24-hr forecast, ranging from 0.3 °C to 0.9 °C. Compared to NoAero, the NCP area-averaged warm bias was remarkably reduced by ~0.40°C (~73.9%) due to aerosol-radiation interaction, with the maximum reaching ~0.54 °C (~95.0 %) at 1100 LT (Figs. 12a and c). Consistently with mean bias, the RMSE was also lower in Aero than NoAero, particularly during 1100 to 2000 LT during the daytime (Figs. 12b and d).

The aerosol-radiation interaction may also have profound impacts on atmospheric structure in addition to radiation and temperature (Rémy et al., 2015). PBLH is one

426 of the key parameters to describe the structure of PBL and closely related to air
427 pollution. It was indicated that the mean daytime PBLH over northern China were
428 around 300–600m (Fig. 13a), and declined generally 40–200m (10%–40%) in Aero
429 over the region with highest $PM_{2.5}$ concentration, particularly over Beijing, Tianjin
430 and Hebei (Figs. 13b–c). As shown in dashed lines in Fig. 14, the NCP
431 area-averaged PBLH at noon-time (1400 LT) was diminished dramatically by
432 aerosol-radiation interaction during the pollution event over northern China, with the
433 maximum decrease reaching -155.2m on 7th Dec. The reduction of PBLH could be
434 the consequence of more stable atmosphere in Aero than NoAero, which was
435 induced by the terrestrial cooling in the lower part of the planetary boundary layer
436 and the solar heat due to the absorbing in the upper layers (solid lines in Fig. 14).
437 The near surface wind fields changes due to aerosol-radiation interaction were
438 further investigated. Figure 15 shows the wind vector in NoAero (upper panel), Aero
439 (middle panel) and their difference (lower panel). It can be seen from Fig. 15a-e that
440 the northern China was dominated by the anticyclonic circulation, accompanied by
441 the relatively weaker northeast wind over Beijing and Hebei areas. The comparisons
442 of Aero and NoAero (Figs. 15 k-o) showed that the northeast wind was increased
443 with the maximum reaching 1 m s^{-1} by aerosol-radiation interaction over Beijing
444 and Hebei, where high particles concentration located (shadings in Figs. 15 f-j).
445 Figures 15k-o also indicated the changes of west wind over the south part of the
446 domain and southeast wind over the ocean areas, which tended to weaken the

anticyclonic circulation and thus declined the wind speed there. The reduced wind speed due the inclusion of aerosol-radiation interaction was possible due to the thermal-wind adjustment in response to the more stable near-surface atmosphere, which was also addressed in previous work using WRF-Chem (Zhang et al., 2015).

The comparisons between simulated wind speeds against in-situ observation averaged during 6th to 10th Dec. were displayed in Fig. 16. In regard of NoAero, the simulated wind speed at 10m was overestimated over the nearly whole domain with the maximum bias up to 3 m s^{-1} except some mountain sites (upper and middle panels in Fig.16). It might be due to the omission of UCM model as the overestimation is more prominent in city clusters (especially in Beijing and southern Hebei) than other areas. Figures 16k-o showed the difference of absolute value of bias between Aero and NoAero and indicated the bias of simulated wind speed were decreased over south and northeast part of the domain during afternoon (Figs. 16k-m) by aerosol-radiation interaction, while were increased over Beijing and Hebei area particularly during nightfall (Fig. 16n) due to the intensified wind speed there. The NCP area-averaged bias and RMSE of wind speed at 10m were further shown in Figure 17. It was seen that the aerosol-radiation interaction helped to reduce the overestimation of wind speed at 10m up to 0.08 m s^{-1} (~7.8%), particular during daytime (Figs. 17a and c). Correspondingly, the RMSE of Aero was also lower than that of NoAero, indicating that the inclusion of aerosol-radiation interaction helped to improve the prediction of near surface wind speed on the domain-averaged scale.

Although the changes of wind speed are less straightforward than that of radiation, the aerosol-radiation interactions can also affect dynamic fields (vertical wind shear) through the changes of atmospheric thermal structure and the thermal wind relation when the interaction lasts long enough (Huang et al., 2019). Figure 18 displayed vertical profiles of wind speed at the stations of Beijing and Xingtai in simulation and verified with sounding observations. It was shown that the NoAero underestimated (overestimated) the low levels wind speed at 0800 LT (2000 LT) at both Beijing and Xingtai. However, the wind speed was increased (decreased) at 0800 LT (2000 LT) in Aero relative to NoAero, indicating the positive impacts on the simulation of atmospheric winds by aerosol-radiation interaction.

Since the forecast meteorological fields by WRF (RMPAS-ST) is routinely applied to WRF-Chem (RMAPS-Chem) as meteorological ICs in the air quality operational system at IUM, the changed meteorology due to aerosol-radiation interaction will further influence the forecast of pollution through meteorological ICs. In regard of further feedback of aerosol-radiation interactions to the transport and dissipation of the pollutants, their impacts on wind field at 850hPa were further discussed as it is strongly correlated with haze formation (Zhang et al., 2018; Zhai et al., 2019). Figures 19 a-e display that northern China was dominated by the anticyclone circulation at 850hPa, associated with the southwest (northwest) wind in the west (east) of the northern part of the domain. The difference of U (zonal, eastward is positive) winds between Aero and NoAero (middle panel in Fig. 16)

showed that the U wind was intensified over west Hebei, accompanied by the quite small changes in Beijing area, indicating that the increased U wind was blocked by the mountains and could not transport the pollutants over Hebei and Beijing to the east (Figs. 19 f-h). On the other hand, the changes of V (meridional, northward is positive) show different patterns over north and south of the 38° N (lower panel in Fig. 19). In the south part, the increased northward wind due to aerosol-radiation interaction may help to transport pollutants from highly polluted areas to Hebei and Beijing. In the north of the domain, the negative (positive) changes of V wind indicated the reduced northward (southward) wind in west (east) of Hebei, which could suppress the diffusion of the pollutants. As a result, both U and V changes induced by the aerosol-radiation interaction will prevent pollutants from dispersing and may exacerbate the pollution in Heibei and Beijing, which confirms the more stable boundary layer due to aerosol-radiation interaction as discussed earlier.

4. Concluding remarks

To facilitate the future inclusion of aerosol-radiation interactions in the regional operational NWP system – RMAPS-ST (adapted from WRF) at IUM, CMA, the impacts of aerosol-radiation interactions on the forecast of surface radiation and meteorological parameters during a heavy pollution event (Dec. 6^{th} -10^{th}, 2015) over northern China were investigated. The aerosol information (550-nm AOD 2D field) were simulated by WRF-Chem and then offline-coupled into RRTMG radiation scheme of WRF to enable the aerosol-radiation feedback in the forecast. Two sets of

24-hour forecasts were performed at 00UTC from Dec. 2^{nd}-11^{th}, 2015. The only difference between the two sets of forecasts was whether the aerosol radiative feedback was activated (Aero, with WRF-Chem simulated hourly AOD fields as input fields) or not (NoAero, no aerosol included), while the other schemes remained the same.

The capability of WRF-chem to reproduce the polluted episode was confirmed first before the offline-coupling of AOD to WRF. The validation of simulated AOD and aerosol extinction coefficient against MODIS and CALIPSO confirmed that the model could reproduce both the spatial and vertical distribution of 550nm AOD. Further results indicated that the temporal variations of simulated AOD at 550nm was in consistent with AERONET and in-situ observation at IAP. In addition, the spatial distributions of $PM_{2.5}$ as well as their magnitude, particularly during the peak stage (8^{th} to 9^{th}) of the pollution event were reasonably captured by WRF-Chem, with the correlation coefficients of 0.85, 0.89, 0.76, 0.92 and 0.77 at Beijing, Shijiazhuang, Tianjin, Hebei and Henan, respectively.

Further, the impacts of aerosols-radiation interaction on the forecasts of surface radiation, energy budget, and meteorology parameters were evaluated against surface and sounding observations. The results showed that the decrease of downward SW radiation reaching surface induced by aerosol effects helped to reduce the overestimation of SW radiation during daytime. Moreover, the simulated surface radiation budget has also been improved, with the biases of net radiation at

surface decreased by 85.3%, 50.0%, 35.4%, and 44.1% during daytime at Beijing, Tianjin, Taiyuan and Jinan respectively, accompanied by the reduction of sensible (16.1 W m^{-2}, 18.5%) and latent (6.8 W m^{-2}, 13.4%) heat fluxes emitted by the surface at noon-time.

The energy budget changed by aerosol extinction further cools 2-m temperature by ~0.40°C over NCP, reducing warm bias by ~73.9% and also leading to lower RMSE, particularly during daytime. Since aerosol cools the lower planetary boundary layer and meanwhile warms the high atmosphere, it induced the more stable stratification of the atmosphere and the declination of PBLH by 40–200m (10%–40%) over NCP. Associating with the changes of planetary boundary structure and more stable near-surface atmosphere, the aerosol-radiation interaction tended to weaken the anticyclonic circulation including the east wind over the south part of the domain and northwest wind over the ocean areas. Thus the bias of wind speed over south and northeast part of the domain were decreased particularly during the afternoon, while increased over Beijing and Hebei area. In regard of NCP-average, the overestimated 10m wind speed was improved during whole day with the maximum up to 0.08 m s^{-1} (~7.8%) at 1400LT. The comparison between simulated vertical profiles of atmospheric wind speed with soundings also indicated that Aero was in better agreement with observation and aerosol-radiation interaction helped to improve the prediction of dynamic fields such as atmospheric wind through the thermal wind relation by altering the atmospheric structure.

552 The impacts of aerosol-radiation interactions on wind field at 850hPa were
553 further discussed. The results showed that aerosol-radiation interaction will prevent
554 pollutants from dispersing and may exacerbate the pollution through changes of both
555 U and V wind, which confirms the more stable boundary layer due to
556 aerosol-radiation. These wind field changes may also influence the forecast of the
557 transport and dissipation of the pollutants by WRF-Chem through changed
558 meteorological ICs.

559 This study analyzed the impacts of aerosol-radiation interaction on radiation and
560 meteorological forecast by using the offline-coupling of WRF and high-frequent
561 updated AOD simulated by WRF-Chem, which is more computationally economic
562 than the online simulation with the integration time for 96h forecast of about 40% of
563 that for online simulation. This approach allows for a potential application to include
564 aerosol-radiation interaction in our current operational NWP systems. The results
565 revealed that aerosol-radiation interaction had profound influence on the
566 improvement of predictive accuracy and the potential prospects for its application in
567 regional NWP in northern China. To verify the statistically significance of the
568 results, we further conducted the 24-hour forecasts for a longer period lasting 27
569 days (Jan. 13th – Feb. 8th, 2017), with no AOD field (NoAero) and WRF-Chem
570 simulated hourly AOD fields (Aero) included, as well as constant AOD value of
571 0.12 (ClimAero), respectively. The results showed that the mean RMSE of 2-m
572 temperature (wind speed at 10m) in Aero and ClimAero relative to NoAero was

reduced by 3.95% (1.86%) and 1.23% (1.63%), respectively (not shown). The one-month results indicated that the simulation with the inclusion of WRF-Chem simulated hourly AOD fields outperformed other two simulations and showed more improvement on the meteorological forecast than the simulation with climatological AOD fields. More detailed evaluations and analysis will be addressed in a future article. As the simulated AOD was adopted in the present study, it should be noted that there exits a discrepancy between simulated AOD and observation in both spatial distribution and temporal variation, which may influence the impacts of aerosol-radiation interaction. Meanwhile, surface energy budget and atmospheric dynamics are also influenced by aerosol-cloud interaction, which are related to cloud microphysical processes and are not discussed in this study.

Data availability Data are available upon request from the first authors Yang Yang (yyang@ium.cn) and corresponding authors Xiujuan Zhao (xjzhao@ium.cn) and Dan Chen (dchen@ium.cn).

Author contribution Yang Yang, Min Chen, Xiujuan Zhao and Dan Chen designed the experiments, Yang Yang and Xiujuan Zhao performed the simulations and carried them out. Yang Yang and Dan Chen prepared the manuscript with contributions from all co-authors.

Competing interests The authors declare that they have no conflict of interest.

Acknowledgments This work was jointly supported by the National Key R&D Program of China (grant nos. 2017YFC1501406 and 2018YFF0300102), Natural Science Foundation of Beijing Municipality (8161004), the National Natural Science Foundation of China (grant nos. 41705076, 41705087 and 41705135), Beijing Major Science and Technology Project (Z181100005418014) and Beijing Natural Science Foundation (grant no. 8204074).

Reference

Ackerman, A. S., Toon, O. B., Stevens, D. E., Heymsfield, A. J., Ramanathan, V., and Welton, E. J.: Reduction of tropical cloudiness by soot, Science, 288, 1042–1047, https://doi.org/10.1126/science.288.5468.1042, 2000.

Baklanov, A., Schlünzen, K., Suppan, P., Baldasano, J., Brunner, D., Aksoyoglu, S., Carmichael, G., Douros, J., Flemming, J., Forkel, R., Galmarini, S., Gauss, M., Grell, G., Hirtl, M., Joffre, S., Jorba, O., Kaas, E., Kaasik, M., Kallos, G., Kong, X., Korsholm, U., Kurganskiy, A., Kushta, J., Lohmann, U., Mahura, A., Manders-Groot, A., Maurizi, A., Moussiopoulos, N., Rao, S. T., Savage, N., Seigneur, C., Sokhi, R. S., Solazzo, E., Solomos, S., Sørensen, B., Tsegas, G., Vignati, E., Vogel, B., and Zhang, Y.: Online coupled regional meteorology chemistry models in Europe: current status and prospects, Atmos. Chem. Phys., 14, 317–398, https://doi.org/10.5194/acp-14-317-2014, 2014.

Chan, C. K. and Yao, X.: Air pollution in mega cities in China, Atmos. Environ., 42, 1–42, https://doi.org/10.1016/j.atmosenv.2007.09.003, 2008.

Chen, D., Liu, Z., Davis, C., and Gu, Y.: Dust radiative effects on atmospheric thermodynamics and tropical cyclogenesis over the Atlantic Ocean using WRF-Chem coupled with an AOD data assimilation system, Atmos. Chem. Phys., 17, 7917–7939, https://doi.org/10.5194/acp-17-7917-2017, 2017.

Chen, F. and Dudhia, J.: Coupling an advanced land surface-hydrology model with the Penn State-NCAR MM5 modeling system. Part I: Model implementation and

623 sensitivity, Mon. Wea. Rev., 129, 569–585, doi:
624 10.1175/1520-0493(2001)129<0569:CAALSH>2.0.CO;2, 2001.
625 Cheng, X., Sun, Z., Li, D., Xu, X., Jia, M., and Cheng, S.: Short-term aerosol
626 radiative effects and their regional difference during heavy haze episodes in
627 January 2013 in China, Atmos. Environ., 165, 248–263,
628 http://dx.doi.org/10.1016/j.atmosenv.2017.06.040, 2017.
629 Cheng, Y. F., Eichler, H., Wiedensohler, A., Heintzenberg, J., Zhang, Y. H., Hu, M.,
630 Herrmann, H., Zeng, L.M., Liu, S., Gnauk, T., Brüggemann, E., and He, L.Y.,
631 Mixing state of elemental carbon and non-light-absorbing aerosol components
632 derived from in situ particle optical properties at Xinken in Pearl River Delta of
633 China, J. Geophys. Res.-Atmos.,111, D20204, doi: 10.1029/2005JD006929,
634 2006.
635 Chou, M. D. and Suarez, M. J.: A solar radiation parameterization for atmospheric
636 studies, Tech. Rep. NASA/TM-1999-104606, 15, Technical Report Series on
637 Global Modeling and Data Assimilation NASA, 1999.
638 Ek, M. B., Mitchell, K. E., Lin, Y., Rogers, E., Grunmann, P., Koren, V., Gayno, G.,
639 and Tarpley, J.D.: Implementation of Noah land surface model advances in the
640 National Centers for Environmental Prediction operational mesoscale Eta model,
641 J. Geophys. Res.-Atmos, 108, 8851, doi:10.1029/2002JD003296, 2003.
642 Elser, M., Huang, R.-J., Wolf, R., Slowik, J. G., Wang, Q., Canonaco, F., Li, G.,
643 Bozzetti, C., Daellenbach, K. R., Huang, Y., Zhang, R., Li, Z., Cao, J.,

644 Baltensperger, U., El-Haddad, I., and Prévôt, A. S. H.: New insights into $PM_{2.5}$
645 chemical composition and sources in two major cities in China during extreme
646 haze events using aerosol mass spectrometry, Atmos. Chem. Phys., 16, 3207–
647 3225, https://doi.org/10.5194/acp-16-3207-2016, 2016.
648 Fan, J., Zhang, R., Tao, W. K., and Mhor, K. I.: Effects of aerosol optical properties
649 on deep convective clouds and radiative forcing, J. Geophys. Res., 113, D08209,
650 doi:10.1029/2007JD009257, 2008.
651 Ghan, S. J., Liu, X., Easter, R. C., Zaveri, R., Rasch, P. J., Yoon, J.-H., Eaton, B.:
652 Toward a Minimal Representation of Aerosols in Climate Models: Comparative
653 Decomposition of Aerosol Direct, Semidirect, and Indirect Radiative Forcing, J.
654 Clim., 2012, 25, 6461-6476, doi: 10.1175/JCLI-D-11-00650.1, 2012.
655 Grell, G. A. and Baklanov, A.: Integrated modelling for forecasting weather and air
656 quality: a call for fully coupled approaches, Atmos. Environ., 45, 6845–6851,
657 https://doi.org/10.1016/j.atmosenv.2011.01.017, 2011.
658 Grell, G. A. and Dévényi, D.: A generalized approach to parameterizing convection
659 combining ensemble and data assimilation techniques, Geophys. Res. Lett., 29,
660 1693, doi: 10.1029/2002GL015311, 2002.
661 Grell, G., Freitas, S. R., Stuefer, M., and Fast, J.: Inclusion of biomass burning in
662 WRF-Chem: impact of wildfires on weather forecasts, Atmos. Chem. Phys., 11,
663 5289-5303, https://doi.org/10.5194/acp-11-5289-2011, 2011.
664 Guo, J., Deng, M., Lee, S. S., Wang, F., Li, Z., Zhai, P., Liu, H., Lv, W., Yao, W., and

665 Li, X.,: Delaying precipitation and lightning by air pollution over the pearl river
666 delta. Part I: observational analyses, J. Geophys. Res.-Atmos, 121, 6472–6488,
667 doi:10.1002/2015JD023257, 2016.
668 Hansen, J., Sato, M., and Ruedy, R.: Radiative forcing and climate response, J.
669 Geophys. Res.-Atmos, 102, 6831–6864, https://doi.org/10.1029/96JD03436,
670 1997.
671 Hong, S.-Y., Noh, Y., and Dudhia, J.: A new vertical diffusion package with an
672 explicit treatment of entrainment processes, Mon. Weather Rev., 134, 2318–2341,
673 doi:10.1175/Mwr3199.1, 2006.
674 Huang, C.-C., Chen, S.-H., Lin, Y.-C., Earl, K., Matsui, T., Lee, H.-H., Tsai, I-C.,
675 Chen, J.-P., and Cheng, C.-T.: Impacts of Dust–Radiation versus Dust–Cloud
676 Interactions on the Development of a Modeled Mesoscale Convective System
677 over North Africa, Mon. Weather Rev., 47, 3301-3326.
678 https://doi.org/10.1175/MWR-D-18-0459.1, 2019.
679 Huang, X., Ding, A., Liu, L., Liu, Q., Ding, K., Niu, X., Nie, W., Xu, Z., Chi, X.,
680 Wang, M., Sun, J., Guo, W., and Fu, C.: Effects of aerosol–radiation interaction
681 on precipitation during biomass-burning season in East China, Atmos. Chem.
682 Phys., 16, 10063–10082, https://doi.org/10.5194/acp-16-10063-2016, 2016.
683 Iacono, M. J., Delamere, J. S., Mlawer, E. J., Shephard, M. W., Clough, S. A.,
684 Collins, W. D.: Radiative forcing by long-lived greenhouse gases: Calculations
685 with the AER radiative transfer models, J. Geophys. Res.-Atmos,113, D13, doi:

686 10.1029/2008JD009944, 2008.
687 Jiang, M., Feng, J., Li, Z., Sun, R., Hou, Y.-T., Zhu, Y., Wan, B., Guo, J., and Cribb,
688 M.: Potential influences of neglecting aerosol effects on the NCEP GFS
689 precipitation forecast, Atmos. Chem. Phys., 17, 13967–13982,
690 https://doi.org/10.5194/acp-17-13967-2017, 2017.
691 Kain, J. S.: The Kain-Fritsch convective parameterization: An update, J. Appl.
692 Meteorol., 43, 170–181, 2004.
693 Kaufman, Y. J., Tanre, D., and Boucher, O.: A satellite view of aerosols in the
694 climate system, Nature, 419, 215-223, http://dx.doi.org/10.1038/nature01091,
695 2002.
696 Liao, H., Chen, W. T., and Seinfeld, J. H.: Role of climate change in global
697 predictions of future tropospheric ozone and aerosols, J. Geophys. Res., 111,
698 D12304, doi:10.1029/2005JD006852, 2006.
699 Liao, L., Lou, S. J., Fu, Y., Chang, W. J., and Liao, H.: Radiative forcing of aerosols
700 andits impact on surface air temperature on the synoptic scale in eastern China,
701 Chinese J. Atmos. Sci. (in Chinese), 39, 68–82.,doi: doi:
702 10.3878/j.issn.1006-9895.1402.13302, 2015.
703 Liu, X., Zhang, Y., Cheng, Y., Hu, M., and Han, T.: Aerosol hygroscopicity and its
704 impact on atmospheric visibility and radiative forcing in Guangzhou during the
705 2006 PRIDE-PRD campaign, Atmos. Environ. 60, 59–67,
706 https://doi.org/10.1016/j.atmosenv.2012.06.016, 2012.

Mlawer, E. J., Taubman, S. J., Brown, P. D., Iacono, M. J. and Clough, S. A.: Radiative transfer for inhomogeneous atmospheres: RRTM, a validated correlated-k model for the longwave, J. Geophys. Res., 102, doi:10.1029/97JD00237. 16663-16682, 1997.

Mulcahy, J. P., Walters, D. N., Bellouin, N., and Milton, S. F.: Impacts of increasing the aerosol complexity in the Met Office global numerical weather prediction model, Atmos. Chem. Phys., 14, 4749–4778, https://doi.org/10.5194/acp-14-4749-2014, 2014.

Oreopoulos, L., Mlawer, E., Delamere, J., Shippert, T., Cole, J., Fomin, B., Iacono, M., Jin, Z., Li, J., Manners, J., Räisä-nen, P., Rose, F., Zhang, Y., Wilson, M. J., and Rossow, W. B.: The Continual Intercomparison of Radiation Codes: Results from Phase I, J. Geophys. Res.-Atmos., 117, D06118, https://doi.org/10.1029/2011JD016821, 2012.

Péré, J. C., Mallet, M., Pont, V., and Bessagnet B.: Impact of aerosol direct radiative forcing on the radiative budget, surface heat fluxes, and atmospheric dynamics during the heat wave of summer 2003 over western Europe: A modeling study, J. Geophys. Res., 116, D23119, https://doi.org/10.1029/2011JD016240, 2011.

Pleim. J. E.: A Combined local and nonlocal closure model for the atmospheric boundary layer. Part I: Model description and testing, J. Appl. Meteorol. Climat., 46, 1383–1395, doi: 10.1175/JAM2539.1, 2007.

Quan, J., Tie, X., Zhang, Q., Liu, Q., Li, X., Gao, Y., and Zhao D.: (2014).

728 Characteristics of heavy aerosol pollution during the 2012–2013 winter in beijing,
729 China, Atmos. Environ., 88, 83-89,
730 https://doi.org/10.1016/j.atmosenv.2014.01.058, 2014.
731 Ramanathan, V., Crutzen, P. J., Kiehl, J. T., and Rosenfeld, D.: Aerosols, Climate
732 and the Hydrological Cycle, Science, 294, 2119–2124, 2001.
733 Rémy, S., Benedetti, A., Bozzo, A., Haiden, T., Jones, L., Razinger, M., Flemming,
734 J., Engelen, R. J., Peuch, V. H., and Thepaut, J. N.: Feedbacks of dust and
735 boundary layer meteorology during a dust storm in the eastern Mediterranean,
736 Atmos. Chem. Phys., 15, 12909–12933,
737 https://doi.org/10.5194/acp-15-12909-2015, 2015.
738 Rodwell, M. J. and Jung T.: Understanding the local and global impacts of model
739 physics changes: an aerosol example, Q. J. Roy. Meteor. Soc., 134, 1479-1497,
740 https://doi.org/10.1002/qj.298, 2008.
741 Rogers, R. E., Deng, A. J., Stauffer, D. R., Gaudet, B. J., Jia, Y. Q., Soong, S. T., and
742 Tanrikulu, S.: Application of the Weather Research and Forecasting Model for Air
743 Quality Modeling in the San Francisco Bay Area, J. Appl. Meteor. Clim., 52,
744 1953–1973, doi: 10.1175/JAMC-D-12-0280.1, 2013.
745 Ruiz-Arias, J. A., Dudhia, J., and Gueymard, C. A.: A simple parameterization of the
746 short-wave aerosol optical properties for surface direct and diffuse irradiances
747 assessment in a numerical weather model, Geosci. Model Dev., 7, 1159–1174,
748 doi:10.5194/gmd-7-1159-2014, 2014.

749 Sekiguchi, A., Shimadera, H., and Kondo, A.: 2018, Impact of Aerosol Direct Effect
750 on Wintertime $PM_{2.5}$ Simulated by an Online Coupled Meteorology-Air Quality
751 Model over East Asia, Aerosol and Air Quality Research, 18: 1068–1079, doi:
752 10.4209/aaqr.2016.06.0282, 2018.
753 Thompson, G., Field, P. R., Rasmussen, R. M., and Hall, W. D.: Explicit forecasts of
754 winter precipitation using an improved bulk microphysics scheme. Part II:
755 Implementation of a new snow parameterization, Mon. Weather Rev., 136, 5095–
756 5115, https://doi.org/10.1175/2008MWR2387.1, 2008.
757 Toll, V., Gleeson, E., Nielsen, K.P., Männik, A., Mašek, J., Rontu, L., and Post, P.:
758 Impacts of the direct radiative effect of aerosols in numerical weather prediction
759 over Europe using the ALADIN-HIRLAM NWP system, Atmos. Res., 172-173,
760 163-173, https://doi.org/10.1016/j.atmosres.2016.01.003, 2016.
761 Toll, V., Reis. K., Ots, R., Kaasik, M., Männik, A., Prank, M., Sofiev, M.: SILAM
762 and MACC reanalysis aerosol data used for simulating the aerosol direct radiative
763 effect with the NWP model HARMONIE for summer 2010 wildfire case in
764 Russia, Atmos. Environ., 121, 75-85,
765 https://doi.org/10.1016/j.atmosenv.2015.06.007, 2015.
766 Wang, H., Shi, G. Y., Zhang, X. Y., Gong, S. L., Tan, S. C., Chen, B., Che, H. Z., and
767 Li, T.: Mesoscale modelling study of the interactions between aerosols and PBL
768 meteorology during a haze episode in China Jing–Jin–Ji and its near surrounding
769 region – Part 2: Aerosols' radiative feedback effects, Atmos. Chem. Phys., 15,

3277-3287, https://doi.org/10.5194/acp-15-3277-2015, 2015b.

Wang, H., Xue, M., Zhang, X. Y., Liu, H. L., Zhou, C. H., Tan, S. C., Che, H. Z., Chen, B., and Li, T.: Mesoscale modeling study of the interactions between aerosols and PBL meteorology during a haze episode in Jing–Jin–Ji (China) and its nearby surrounding region – Part 1: Aerosol distributions and meteorological features, Atmos. Chem. Phys., 15, 3257–3275, https://doi.org/10.5194/acp-15-3257-2015, 2015a.

Wang, J., Wang, S., Jiang, J., Ding, A., Zheng, M., Zhao, B., Wong, D. C., Zhou, W., Zheng, G., Wang, L., Pleim, J. E. and Hao, J.: Impact of aerosol–meteorology interactions on fine particle pollution during China's severe haze episode in January 2013, Environ. Res. Lett., 9, 094002, doi:10.1088/1748-9326/9/9/094002, 2014.

Wang, X, He, X., Miao, S., Dou, Y.: Numerical simulation of the influence of aerosol radiation effect on urban boundary layer, Sci. China Earth Sci., 61, 1844–1858, https://doi.org/10.1007/s11430-018-9260-0, 2018.

Yang, X., Zhao, C., Zhou, L., Wang, Y., Liu, X.: Distinct impact of different types of aerosols on surface solar radiation in China, J. Geophys. Res.-Atmos., 121, 6459-6471, doi: 10.1002/2016JD024938, 2017b.

Yang, Y. and Ren, R. C.: On the contrasting decadal changes of diurnal surface temperature range between the Tibetan Plateau and southeastern China during the 1980s–2000s, Adv. Atmos. Sci., 34, 181–198, doi: 10.1007/s00376-016-6077-z,

2017a.

Yu, H., Kaufman, Y. J., Chin, M., Feingold, G., Remer, L. A., Anderson, T. L., Balkanski, Y., Bellouin, N., Boucher, O., Christopher, S., DeCola, P., Kahn, R., Koch, D., Loeb, N., Reddy, M. S., Schulz, M., Takemura, T., and Zhou, M.: A review of measurement-based assessments of the aerosol direct radiative effect and forcing, Atmos. Chem. Phys., 6, 613-666, https://doi.org/10.5194/acp-6-613-2006, 2006.

Zaveri, R. A. and Peters, L. K.: A new lumped structure photochemical mechanism for large-scale applications, J. Geophys. Res., 104, 30387–30415, https://doi.org/10.1029/1999JD900876,1999.

Zhai, S., Jacob, D. J., Wang, X., Shen, L., Li, K., Zhang, Y., Gui, K., Zhao, T., and Liao, H.: Fine particulate matter ($PM_{2.5}$) trends in China, 2013–2018: separating contributions from anthropogenic emissions and meteorology, Atmos. Chem. Phys., 19, 11031-11041, https://doi.org/10.5194/acp-19-11031-2019, 2019.

Zhang, B., Wang, Y., and Hao, J.: Simulating aerosol–radiation–cloud feedbacks on meteorology and air quality over eastern China under severe haze conditionsin winter, Atmos. Chem. Phys., 15, 2387-2404, https://doi.org/10.5194/acp-15-2387-2015, 2015.

Zhang, Q., Ma, Q., Zhao, B., Liu, X., Wang, Y., Jia, B., and Zhang, X.: Winter haze over North China Plain from 2009 to 2016: Influence of emission and meteorology, Environ. Pollut., 242, 1308–1318.

812 doi:10.1016/j.envpol.2018.08.019, 2018.
813 Zhang, Q., Quan, J., Tie, X., Li, X., Liu, Q., Gao, Y., and Zhao, D. L.: Effects of
814 meteorology and secondary particle formation on visibility during heavy haze
815 events in Beijing, China, Sci. Total Environ., 502, 578–584,
816 https://doi.org/10.1016/j.scitotenv.2014.09.079, 2015.
817 Zhang, Y., Wen, X.-Y., and Jang, C.-J.: Simulating
818 chemistry-aerosol-cloud-radiation-climate feedbacks over the continental U.S.
819 using the online-coupled Weather Research Forecasting Model with chemistry
820 (WRF/Chem), Atmos. Environ. 44, 3568–3582,
821 https://doi.org/10.1016/j.atmosenv.2010.05.056, 2010.
822 Zhang, Y.-Z, Miao, S.-G., Dai, Y.-J., Liu, Y.-H., Numerical simulation of
823 characteristics of summer clear day boundary layer in Beijing and the impact of
824 urban underlying surface on sea breeze (in Chinese), Chin J. Geophys, 56,
825 2558–2573, 2013.
826 Zhao, X., Li, Z., Xu, J.: Modification and performance tests of visibility
827 parameterizations for haze days, Environ. Sci., 40, 1688-1696 (in Chinese), 2019.
828 Zheng, Y., Che, H., Xia, X., Wang, Y., Wang, H., Wu, Y., Tao, J., Zhao, H., An, J.,
829 Li, L., Gui, K., Sun, T., Li, X., Sheng, Z., Liu, C., Yang, X., Liang, Y., Zhang, L.,
830 Liu, C., Kuang, X., Luo, S., You, Y., and Zhang, X.: Five-year observation of
831 aerosol optical properties and its radiative effects to planetary boundary layer
832 during air pollution episodes in North China: Intercomparison of a plain site and

833 a mountainous site in Beijing, Sci. Total Environ., 674, 140–158.
834 https://doi.org/10.1016/j.scitotenv.2019.03.418, 2019.

835 Table 1. The variables, sources, numbers of sites in the domain/NCP and the

836 frequency of chemical and meteorological observations.

Variables	Source of observation	Numbers of sites over the domain/NCP	Frequency	locations
AOD	AERONET	3/3	hourly	black dots in Fig. 1b
AOD	IAP station	1/1	hourly	blue dot in Fig. 1b
AOD	MODIS	/	daily	Fig. 2f-j and Fig. 2p-t
aerosol extinction coefficient	CALIPSO	/	daily	black paths in Fig.3a-d
$PM_{2.5}$	China National Environmental Monitoring Centre	813/332	hourly	dots in Fig. 5a
radiation	China Meteorological Administration	4/4	hourly	triangles in Fig. 1a
radiation	IAP station	1/1	hourly	triangles in Fig. 1a
2-m temperature	China Meteorological Administration	1157/534	hourly	dots in Fig. 11a
wind at 10m	China Meteorological Administration	1157/534	hourly	dots in Fig. 11a
atmospheric wind	China Meteorological Administration	2/2	0800LT, 2000LT	circles in Fig. 1a

837

838 Table 2. Mean bias of downward SW radiation at surface (W m^{-2}) and Net radiation
839 at surface (W m^{-2}) from NoAero and Aero relative to observation during daytime
840 (averaged 0800 to 1800 LT) and nighttime (averaged 1900 to 0700 LT), averaged
841 from 6th to 11th Dec. 2015 at Beijing, Tianjin, Taiyuan and Jinan respectively.

842

Station	SW radiation		Net radiation			
	Daytime		Daytime		Nighttime	
	NoAero	Aero	NoAero	Aero	NoAero	Aero
Beijing	149.4	38.0	102.2	15.0	-33.6	-33.2
Tianjin	115.5	70.9	72.2	36.4	-27.1	-26.4
Taiyuan	155.0	118.3	66.9	43.2	-33.6	-33.3
Jinan	149.1	97.7	81.2	45.3	-30.3	-29.3

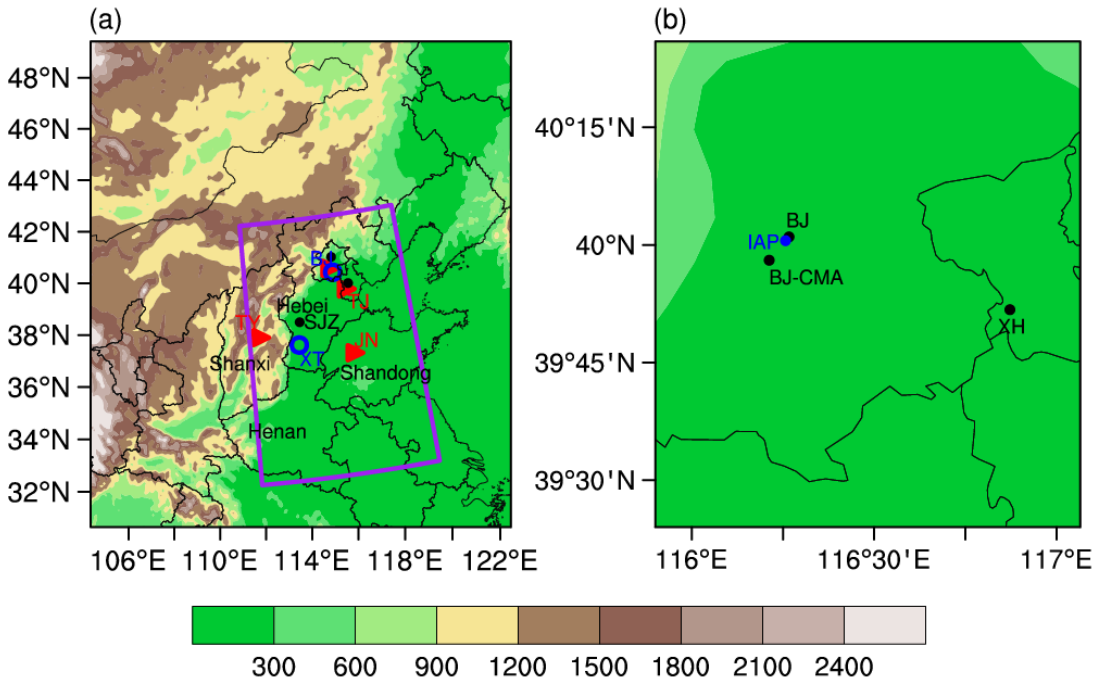

843

844 Figure 1. (a) The model domain and the terrain height (shadings, m). Purple box

845 denotes the NCP, triangles are the observational sites of radiation (BJ: Beijing, TJ:

846 Tianjin, TY: Taiyuan and JN: Jinan), circles are sites of sounding observation (BJ:

847 Beijing and XT: Xingtai), dots denote the major cities for validation of $PM_{2.5}$ (BJ:

848 Beijing, SJZ: Shijiazhuang and TJ: Tianjin). Names of provinces are also added

849 (Hebei, Shanxi, Shandong and Henan). (b) The observational sites of AOD,

850 including AERONET sites (black dots, BJ: Beijing, BJ-CMA: Beijing-CMA and XH:

851 Xianghe) and IAP in-situ (blue dot) site.

852

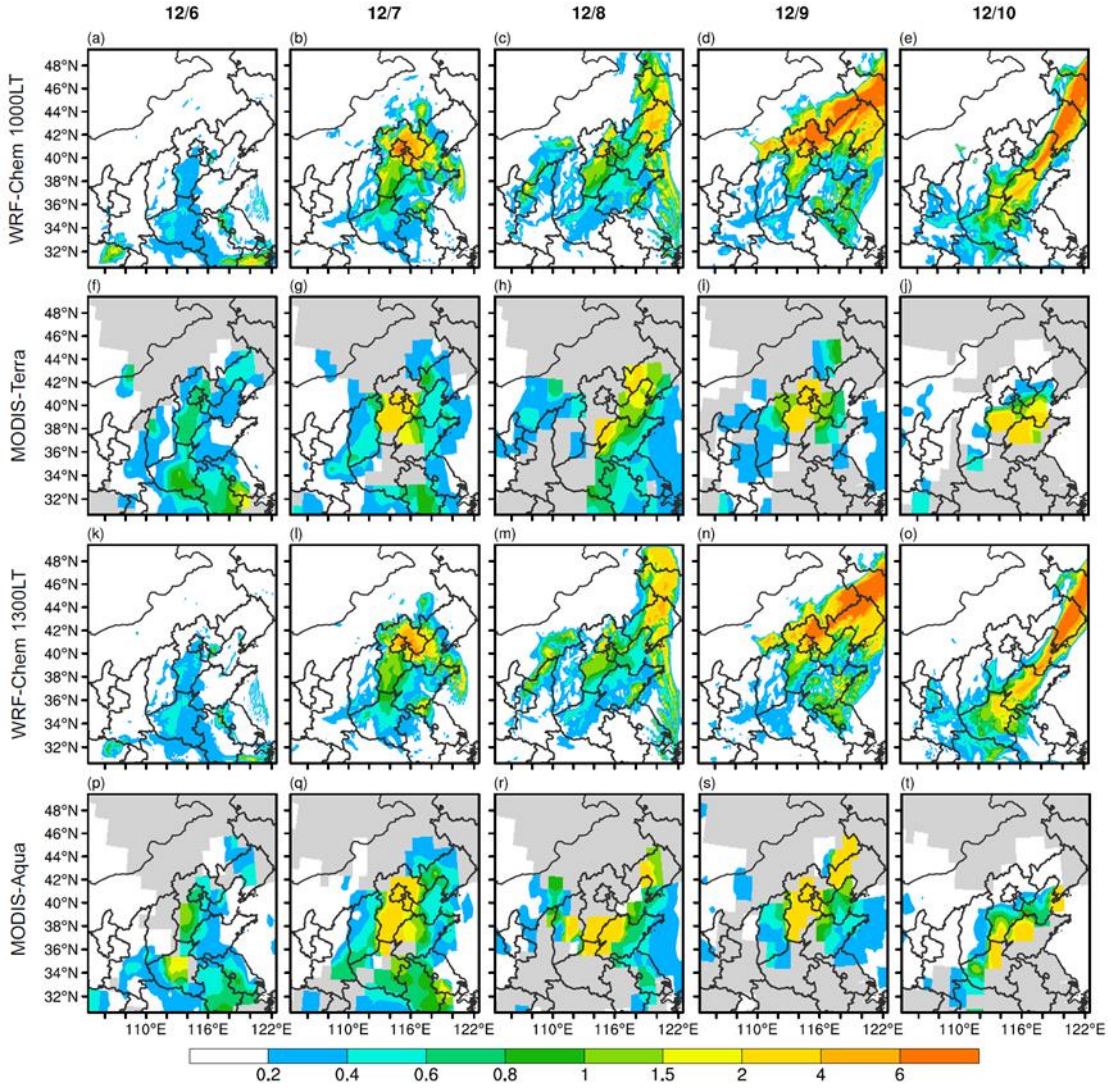

853

854 Figure 2. The WRF-Chem simulated and MODIS observed spatial distribution of

855 AOD on 6th-10th December (from left to right). The first (a-e) and third rows (k-o)

856 are WRF-Chem simulations at 1000LT and 1300LT (MODIS path times)

857 respectively. The second (f-j) and fourth (p-t) rows are MODIS Terra and Aqua

858 observations, respectively. Gray areas in (f-j) and (p-t) denote the missing values.

859

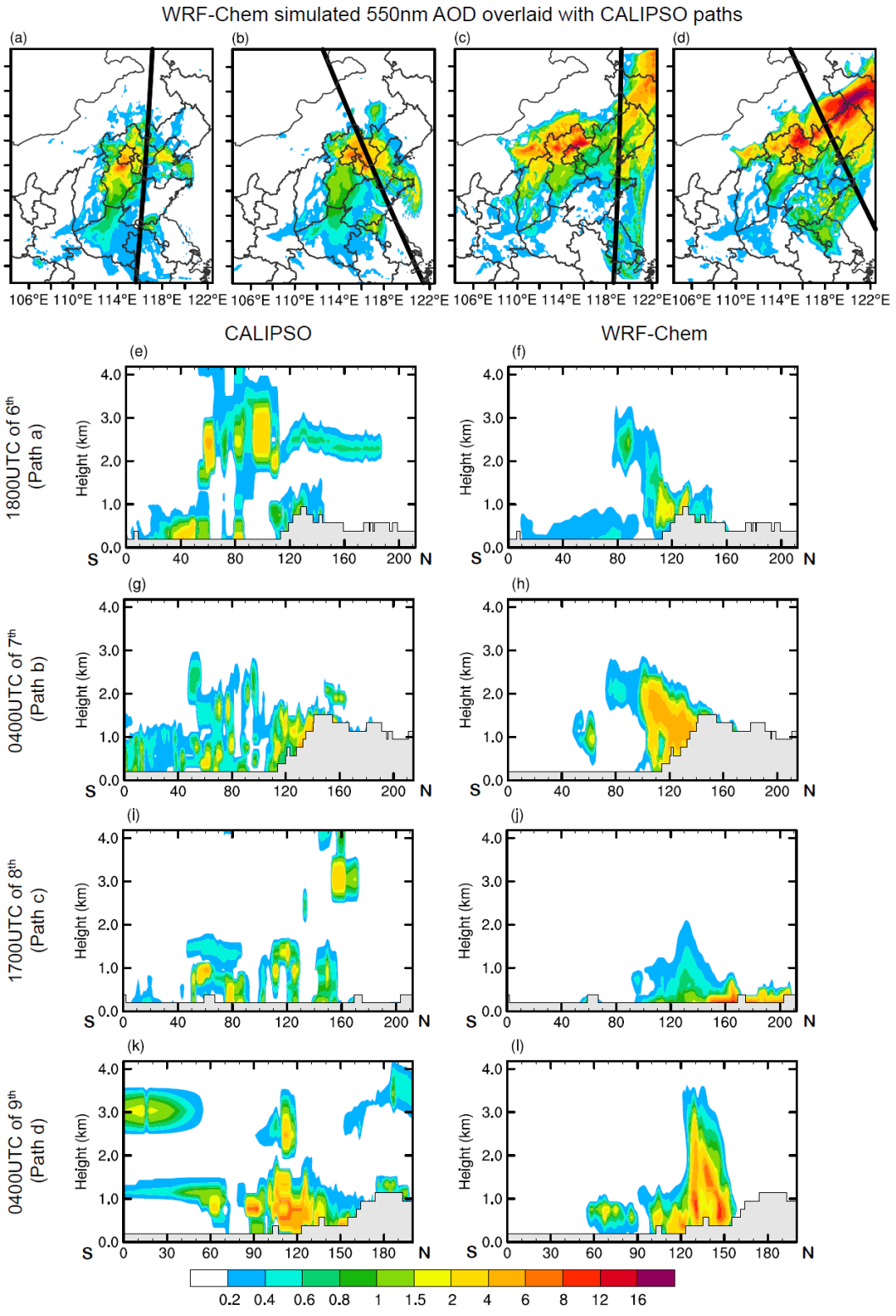

Figure 3. The WRF-Chem simulated 550nm AOD (shadings) on (a)1800UTC of 6th, (b) 0400UTC of 7th, (c)1700UTC of 8th, (d) 0400UTC of 9th December overlaid with CALIPSO paths (black thick solid). (e-l) denote the corresponding vertical

distributions of aerosol extinction coefficient at 550nm from (e, g, i, k) CALIPSO and (f, h, j, l) model simulations. Gray areas in (e-l) denote the terrain.

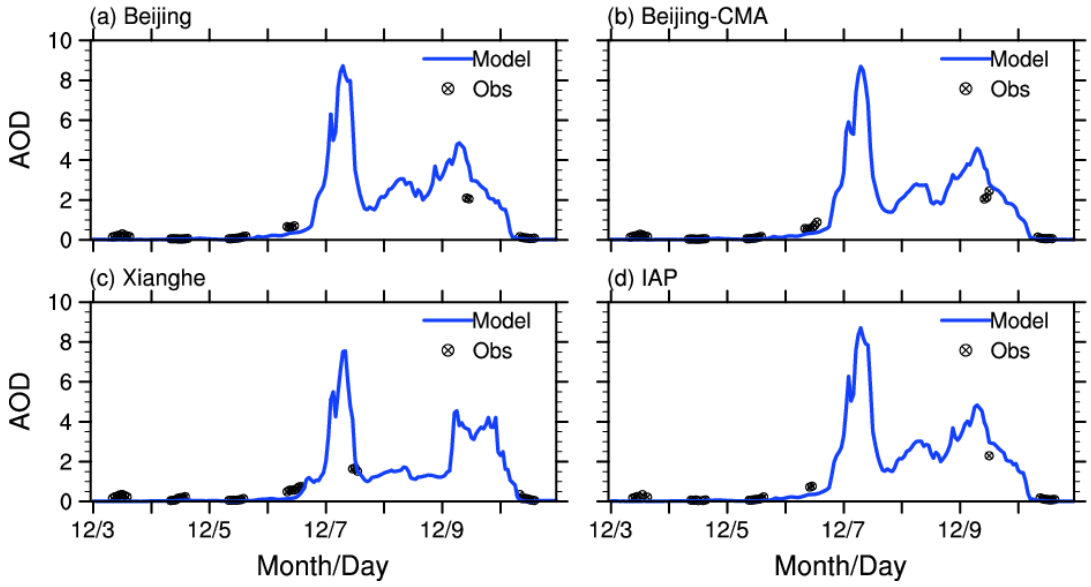

867

868 Figure 4. Temporal variation of observed (black dots) and simulated (blue) AOD at

869 550nm during 3rd-10th Dec. (LT) at (a) Beijing, (b) Beijing-CMA, (c) Xianghe and (d)

870 IAP, AOD observations are from (a-c) AERONET and (d) IAP in-situ site.

871

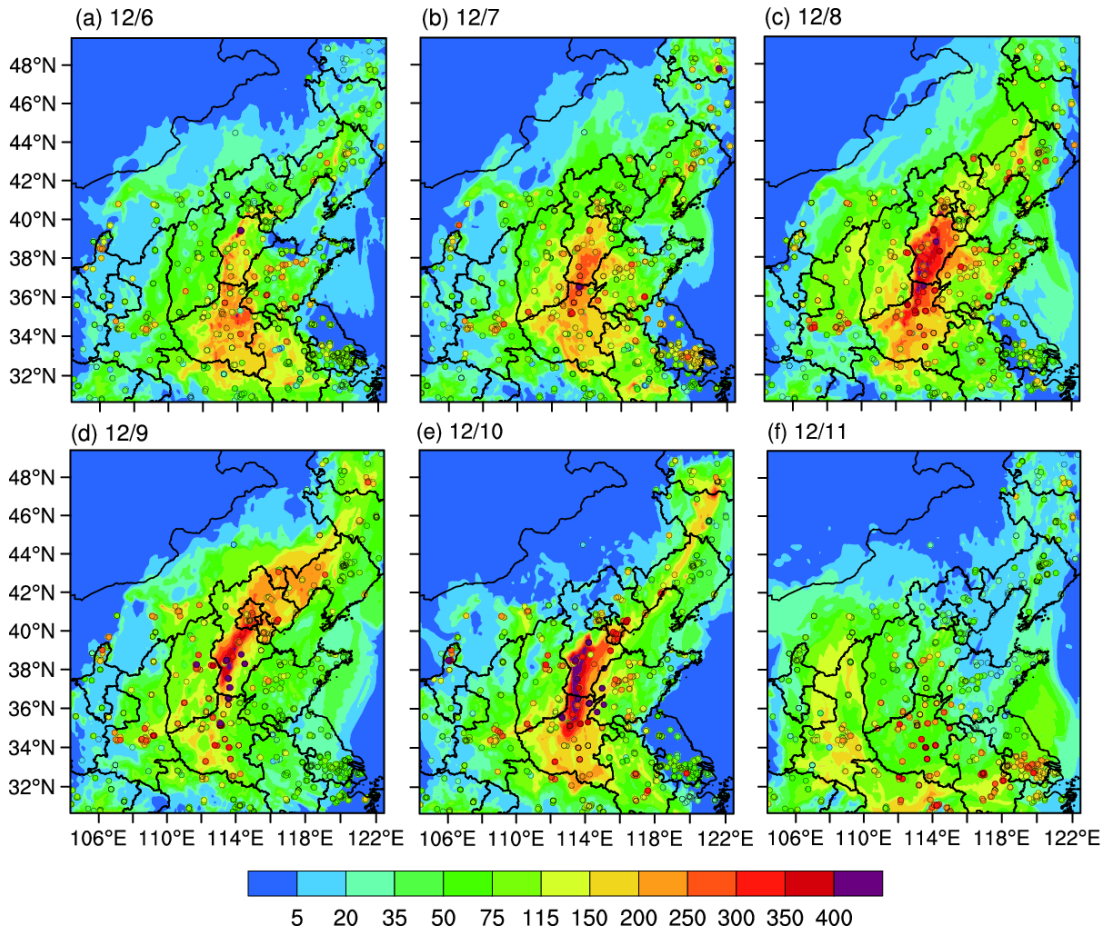

872

873 Figure 5. Observed (colored dots) and WRF-Chem simulated (shadings) spatial

874 distribution of $PM_{2.5}$ concentrations ($\mu g\ m^{-3}$) on 0800LT of (a) 6th, (b) 7th, (c) 8th, (d)

875 9th, (e) 10th and (f) 11th Dec. respectively.

876

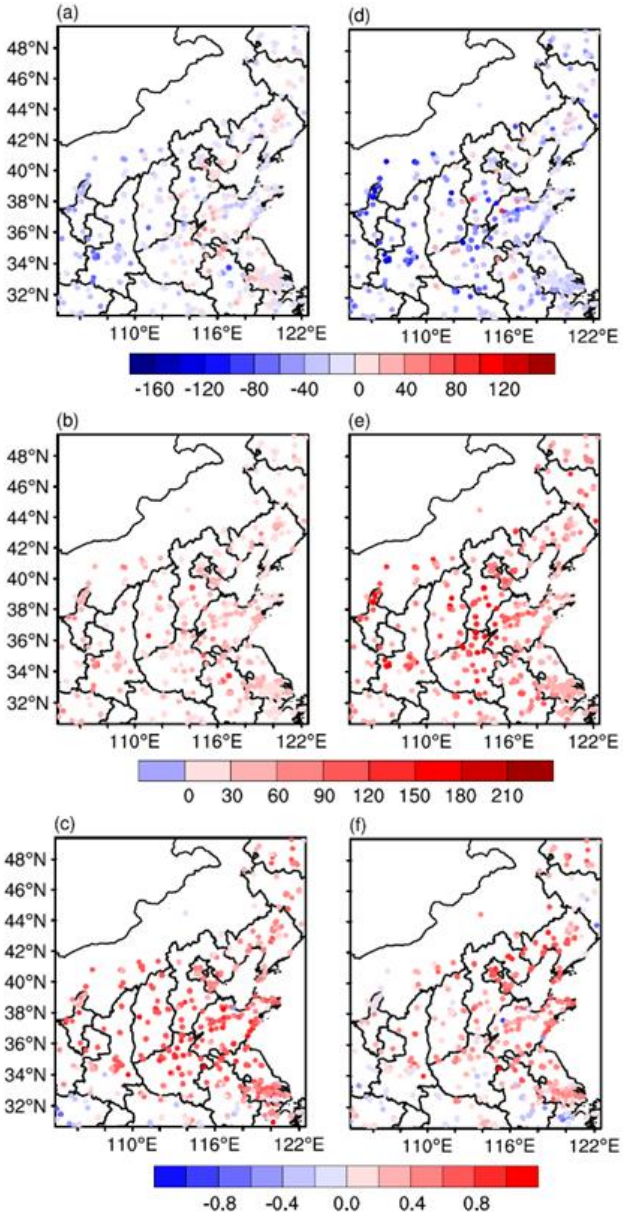

877

878 Figure 6. The (a, d) bias (μg m^{-3}), (b, e) RMSE (μg m−3), and (c, f) correlation

879 coefficient (1) averaged (a-c) during clean period (3th to 5th Dec.) and (d-f) the

880 polluted period (6th to 10th December).

881

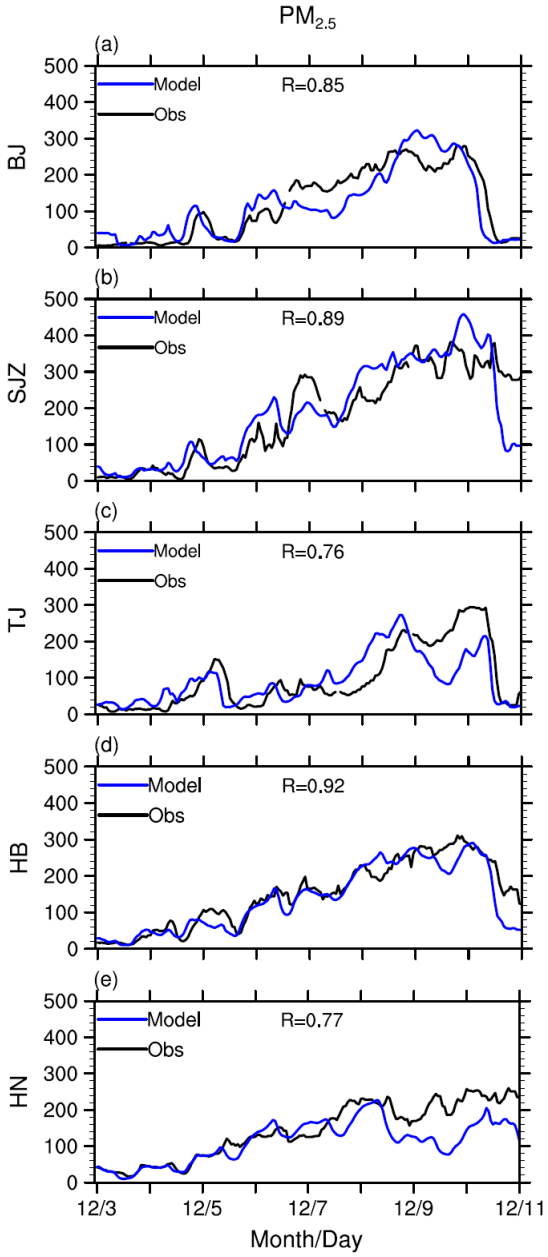

882

883 Figure 7. Observed (black) and WRF-Chem simulated (blue) temporal variation of

884 $PM_{2.5}$ (μg m^{-3}) at three major cities (a) Beijing (BJ), (b) Shijiazhuang (SJZ)

885 (c)Tianjin (TJ) and two provinces (d) Hebei (HB) and (e) Henan (HN).

886

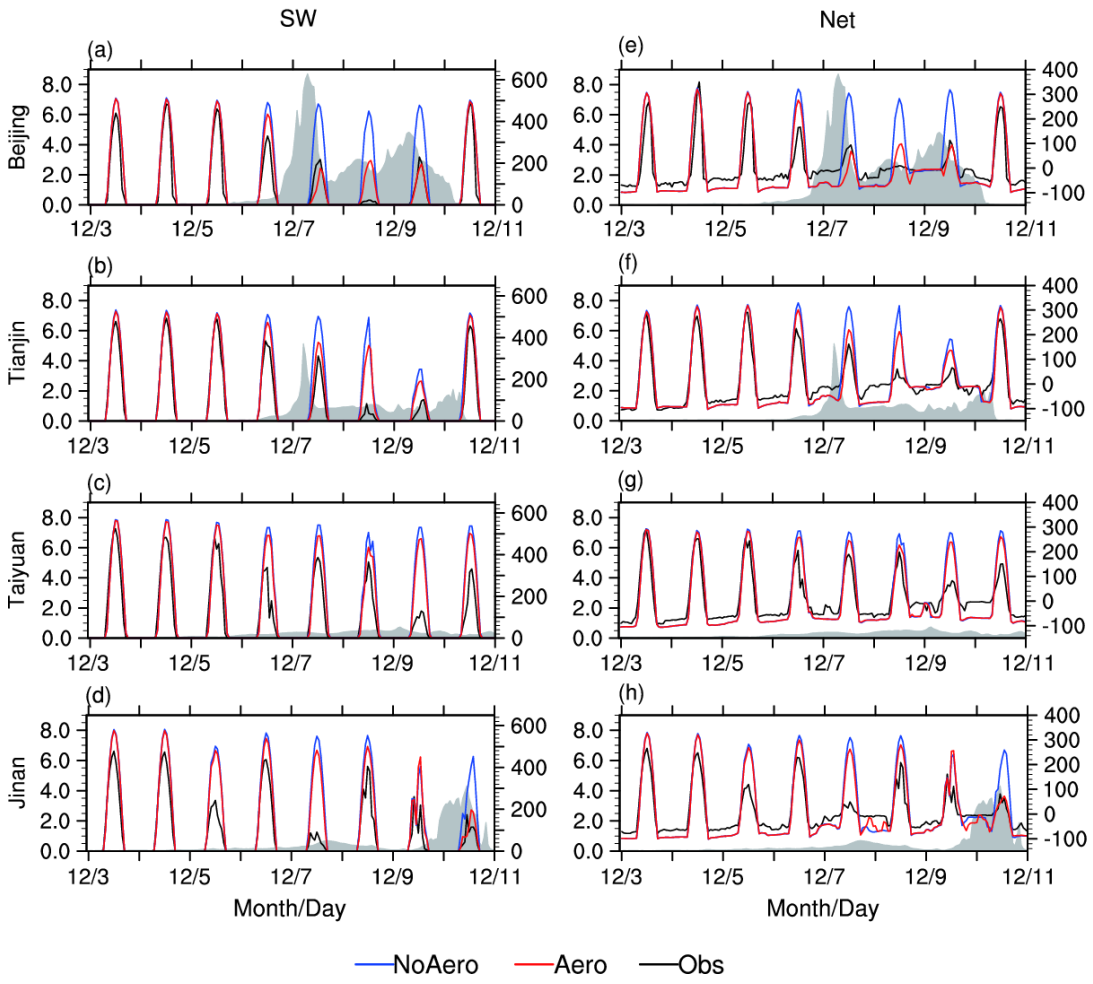

887

888 Figure 8. (a–d) observed (black) and WRF simulated (NoAero: blue, Aero: red)

889 temporal variation of downward shortwave radaition at surface (W m^{-2}, right axis)

890 at (a) Beijing, (b) Tianjin, (c) Taiyuan and (d) Jinan, respectively. The grey areas

891 indicate the simulated AOD (left axis) by WRF-Chem. (e–h) are same with (a–d),

892 but for net radaition at surface (W m^{-2}).

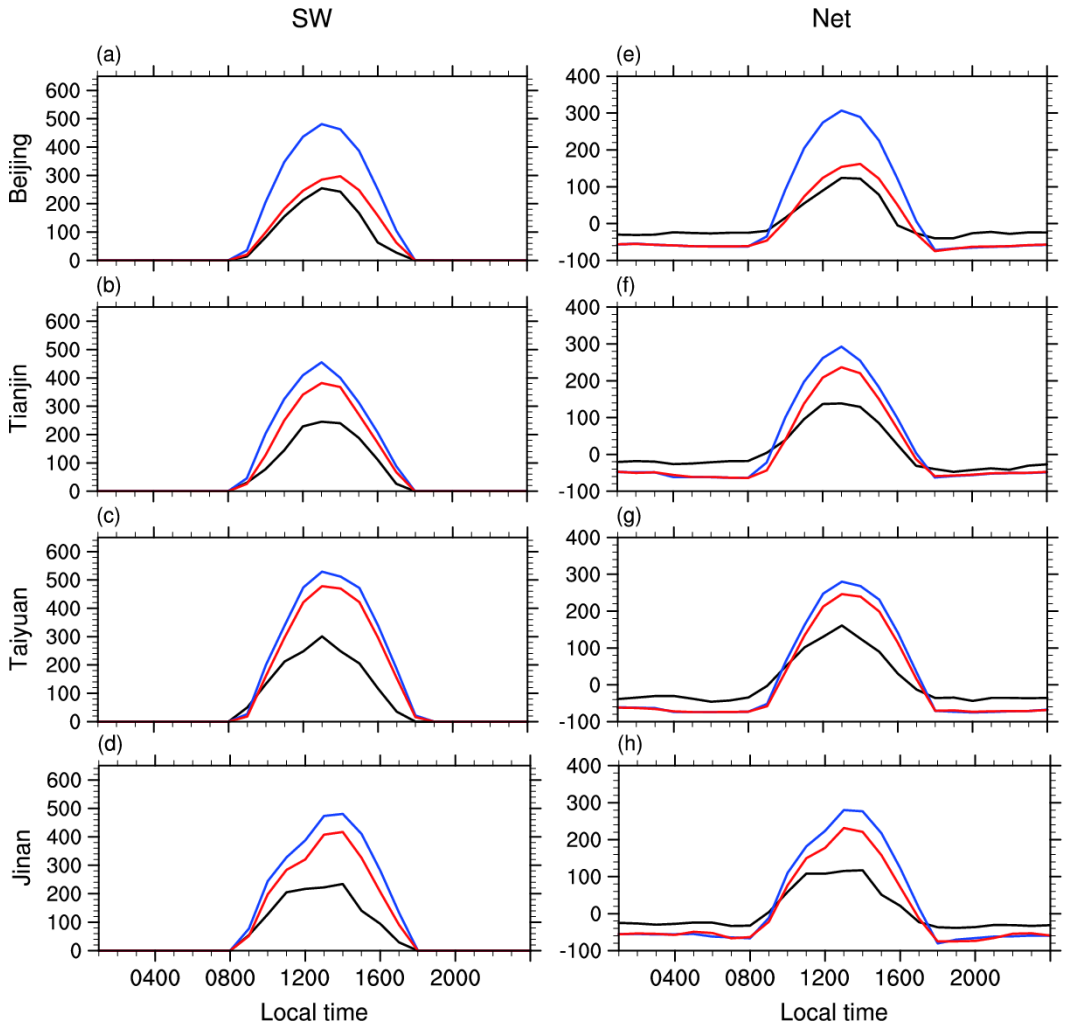

Figure 9. (a–d) observed (black) and simulated (NoAero: blue, Aero: red) diurnal cycles of downward shortwave radaition at surface (W m^{-2}) averaged from 6th to 10th Dec. 2015 at (a) Beijing, (b) Tianjin, (c) Taiyuan and (d) Jinan, respectively. (e–h) are same with (a–d), but for net radaition at surface (W m^{-2}).

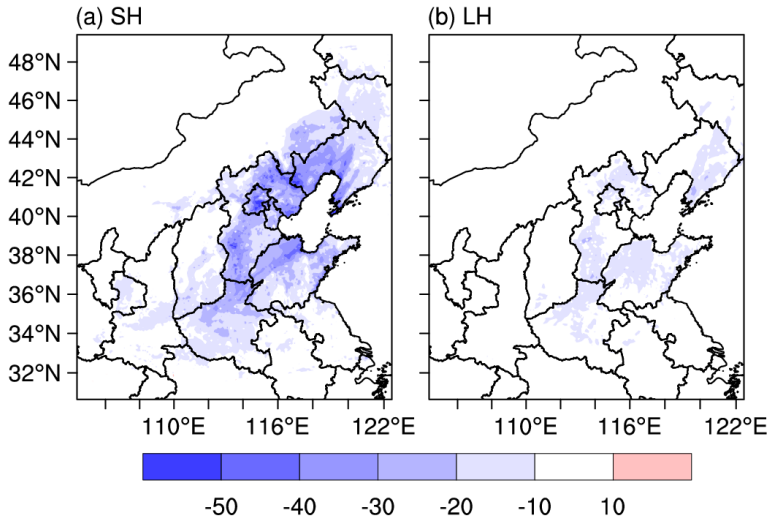

898

899 Figure 10. The differences (Aero minus NoAero) of (a) surface sensible heat flux

900 and (b) surface latent heat flux (W m^{-2}, upward is positive) at 1300LT averaged

901 from 6th to 10th Dec. 2015.

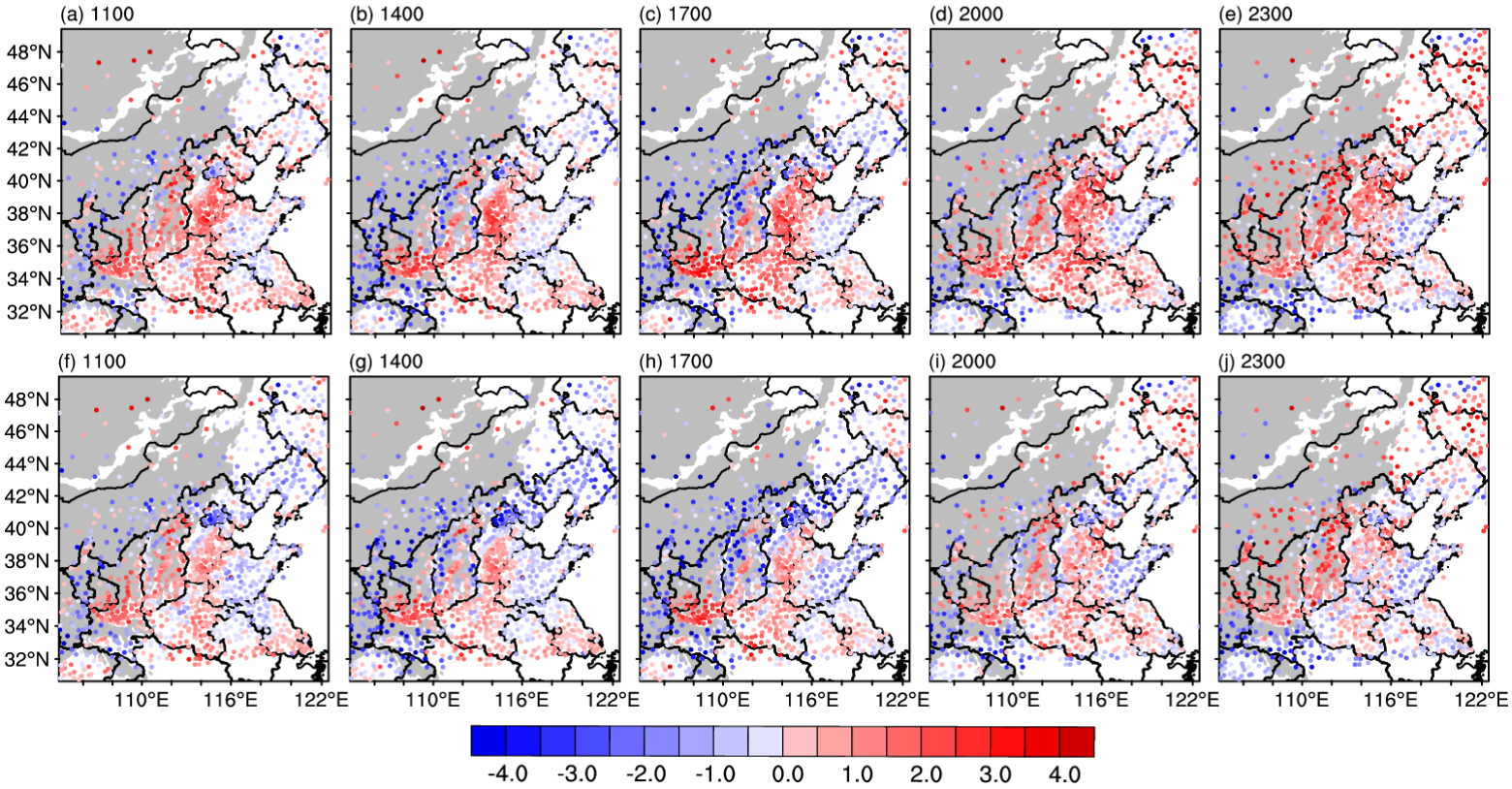

902

903 Figure 11. The bias of 2-m temperature (°C) at (a) 1100, (b) 1400, (c) 1700, (d) 2000 and (e) 2300 LT in NoAero averaged from 6th to 10th Dec.

904 2015, (f–j) are same with (a–e), but for Aero. The grey areas denote the areas of terrain height above 1000m.

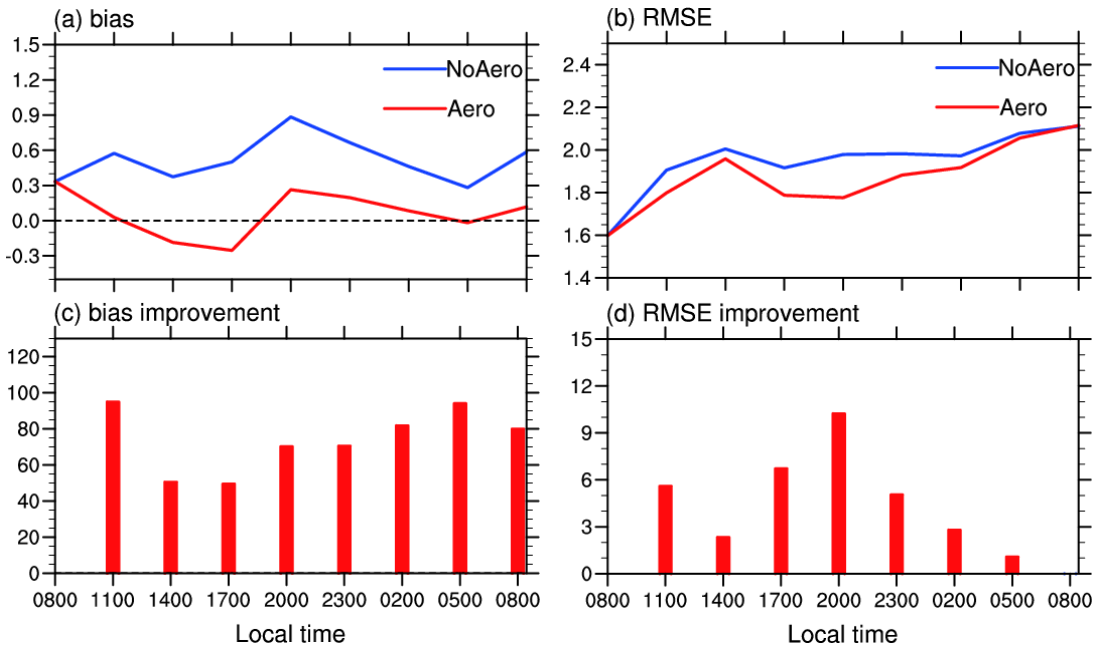

Figure 12. Area-averaged (a) bias and (b) RMSE of simulated 2-m temperature (°C) in NoAero (blue) and Aero (red) over NCP area (defined in Fig. 1a), averaged from 6th to 10th Dec. 2015, and the mean improvement (%) of (c) absolute value of bias and (d) RMSE in Aero relative to NoAero.

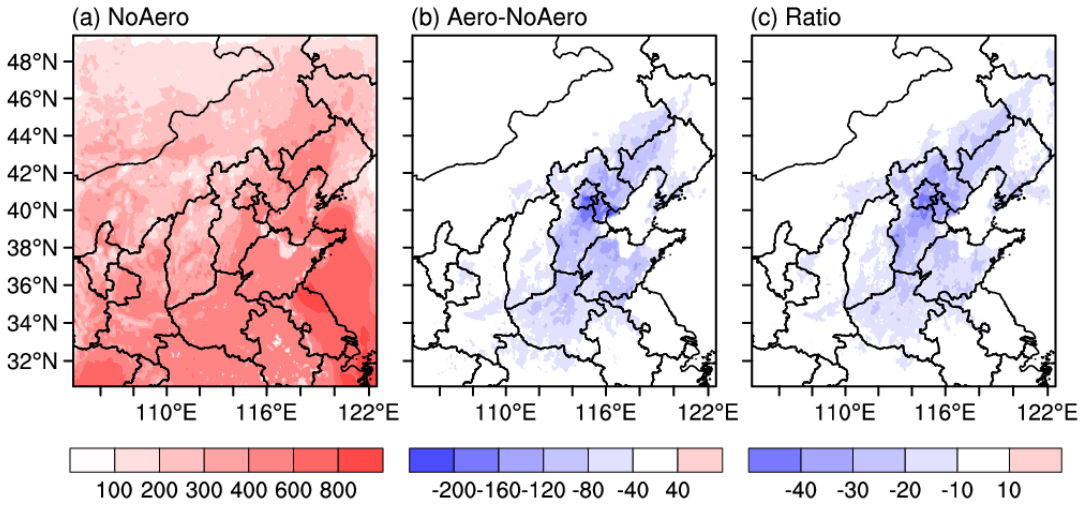

910

911 Figure 13. Daytime mean PBLH (m) in NoAero, (b) the difference between Aero

912 and NoAero (Aero minus NoAero) and (c) the ratio of changes (%) averaged during

913 6th to 10th Dec. 2015.

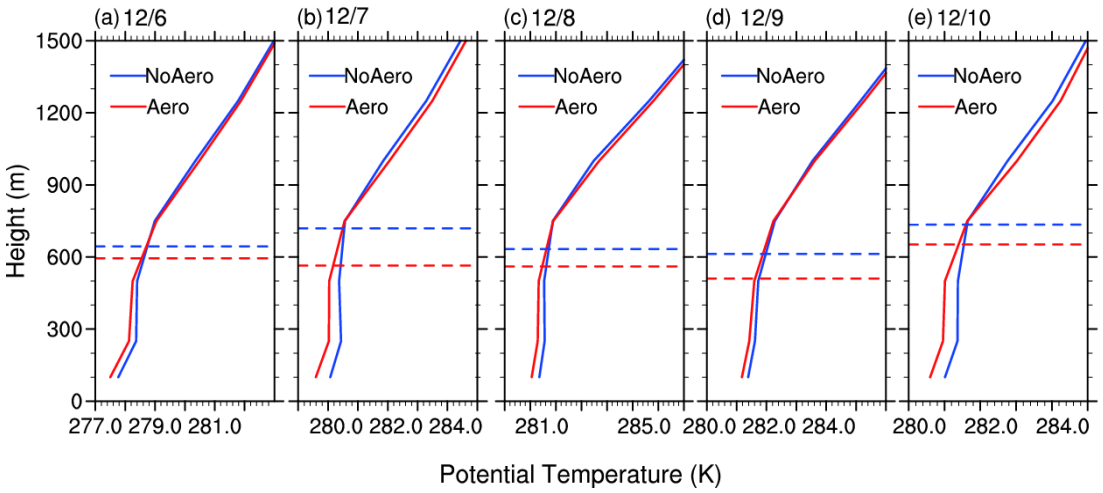

914

915 Figure 14. NCP (defined in Fig. 1a) area-averaged vertical profiles of potential

916 temperature (K, solid) and planetary boundary-layer height (m, dash) in NoAero

917 (blue) and Aero (red) at 1400 LT of (a) 6th, (b) 7th, (c) 8th, (d) 9th and (e) 10th Dec.

918 2015.

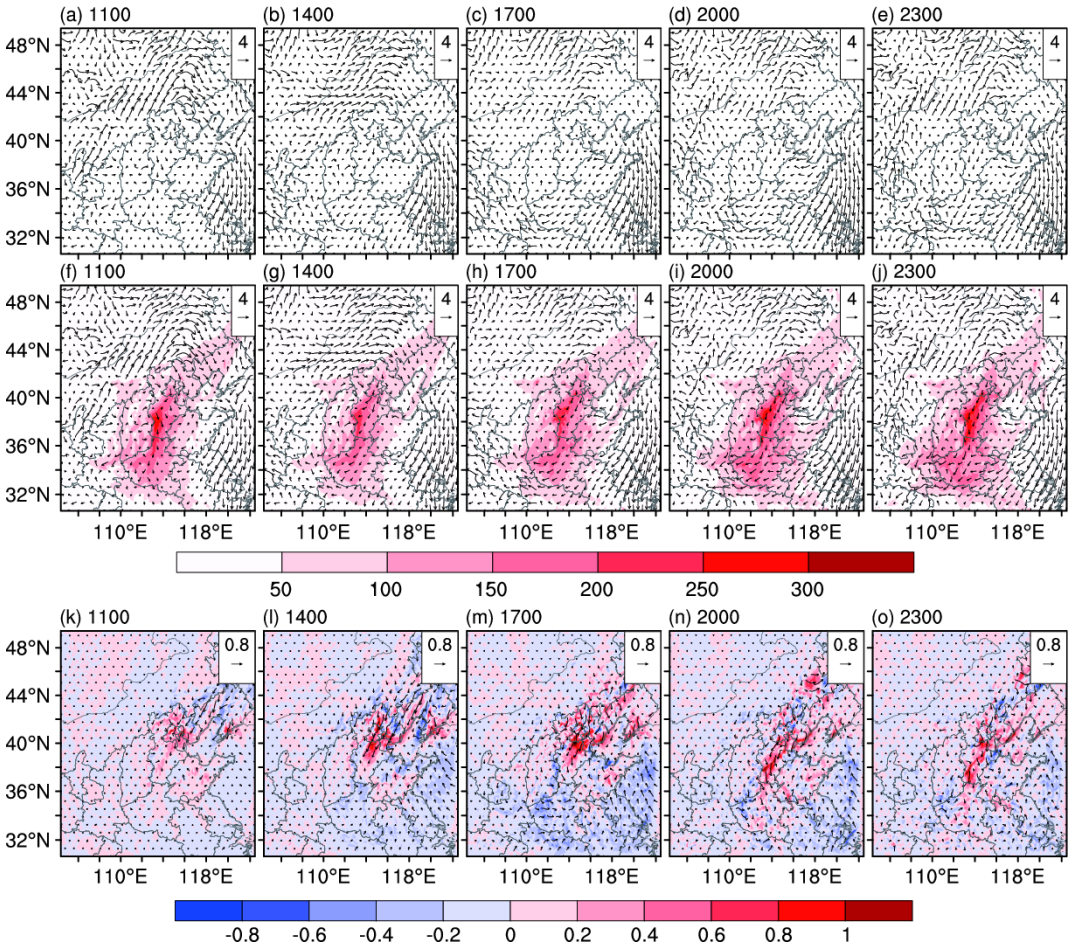

Figure 15. The 10m wind (vector) at 1100, 1400, 1700, 2000 and 2300 LT in (a–e) NoAero and (f–j) Aero averaged during 6th to 10th Dec. 2015, shadings in (f–j) are simulated $PM_{2.5}$ concentrations (μg m^{-3}). (k–o) the difference of 10m wind (vector) and wind speed (shadings) between Aero and NoAero (Aero minus NoAero).

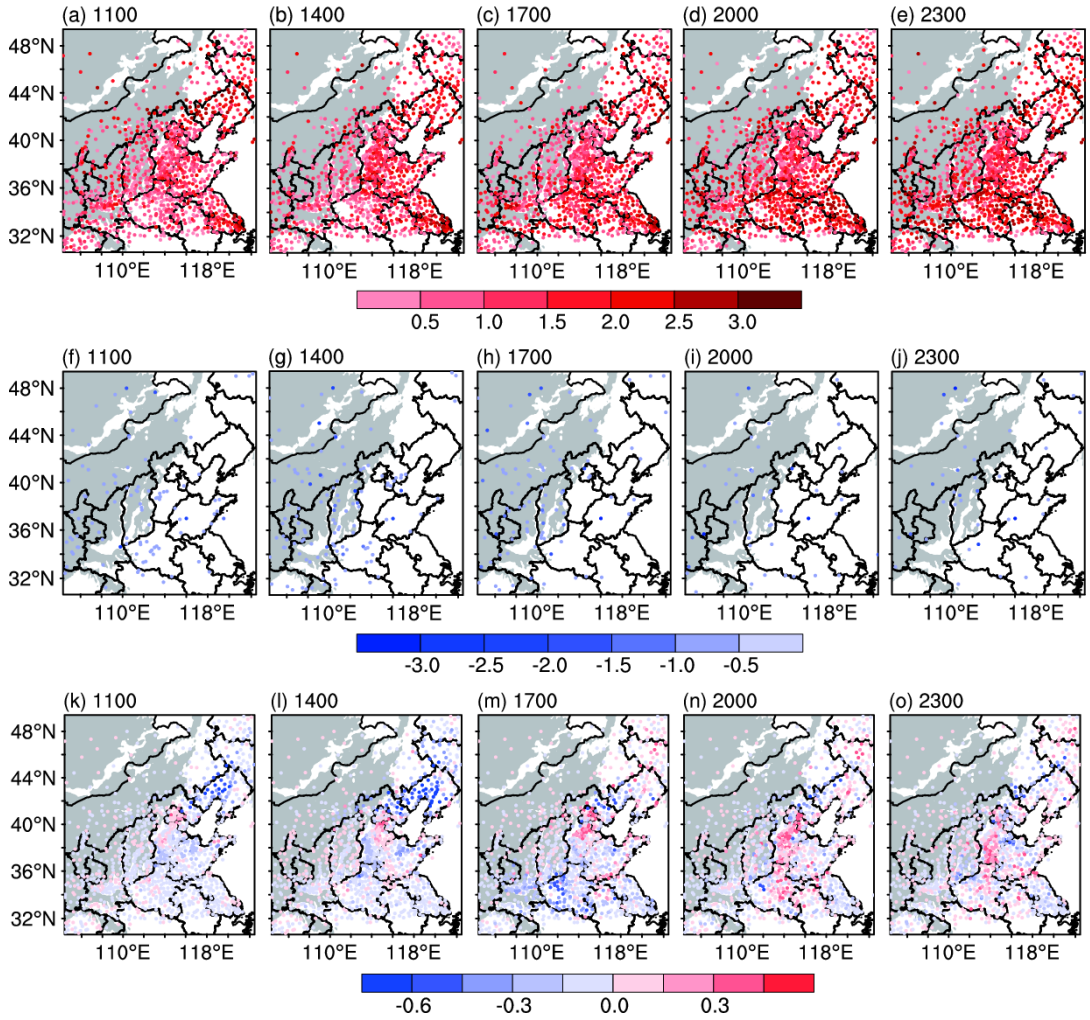

924

925 Figure 16. The bias of 10m wind speed (m s^{-1}) at 1100, 1400, 1700, 2000 and 2300

926 LT for (a–e) overestimated sites and (f–j) underestimated sites in NoAero averaged

927 during 6th to 10th Dec. 2015. (k–o) the difference of absolute value of bias (m s^{-1})

928 between Aero and NoAero (Aero minus NoAero). The grey areas denote the areas of

929 terrain height above 1000m.

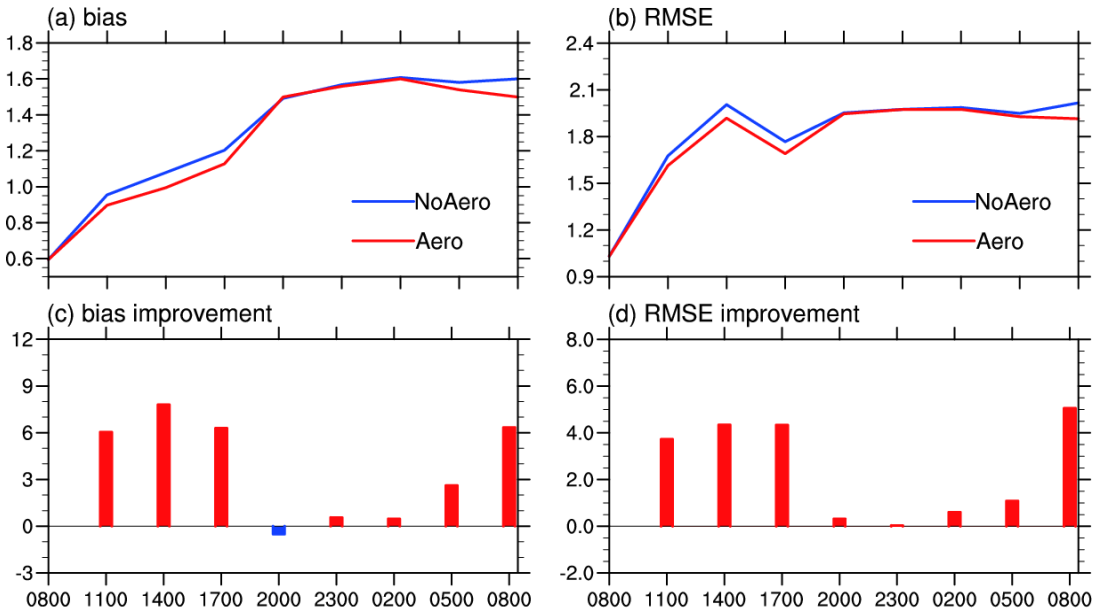

930

931 Figure 17. Same with Fig.12, but for wind speed at 10m (m s^{-1}).

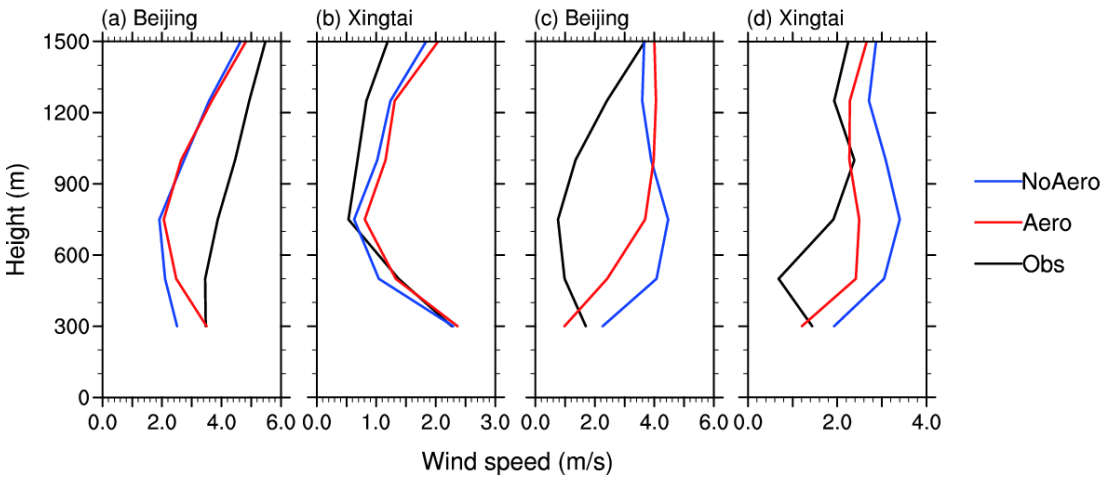

932

933 Figure 18. (a–b) Observed (black) and simulated (NoAero: blue, Aero: red) vertical

934 profiles of atmospheric wind speed (m s^{-1}) at (a) Bejing and (b)Xingtai at 0800LT

935 averaged from 6th to 10th Dec., (c–d) are same with (a–b), but at 2000LT.

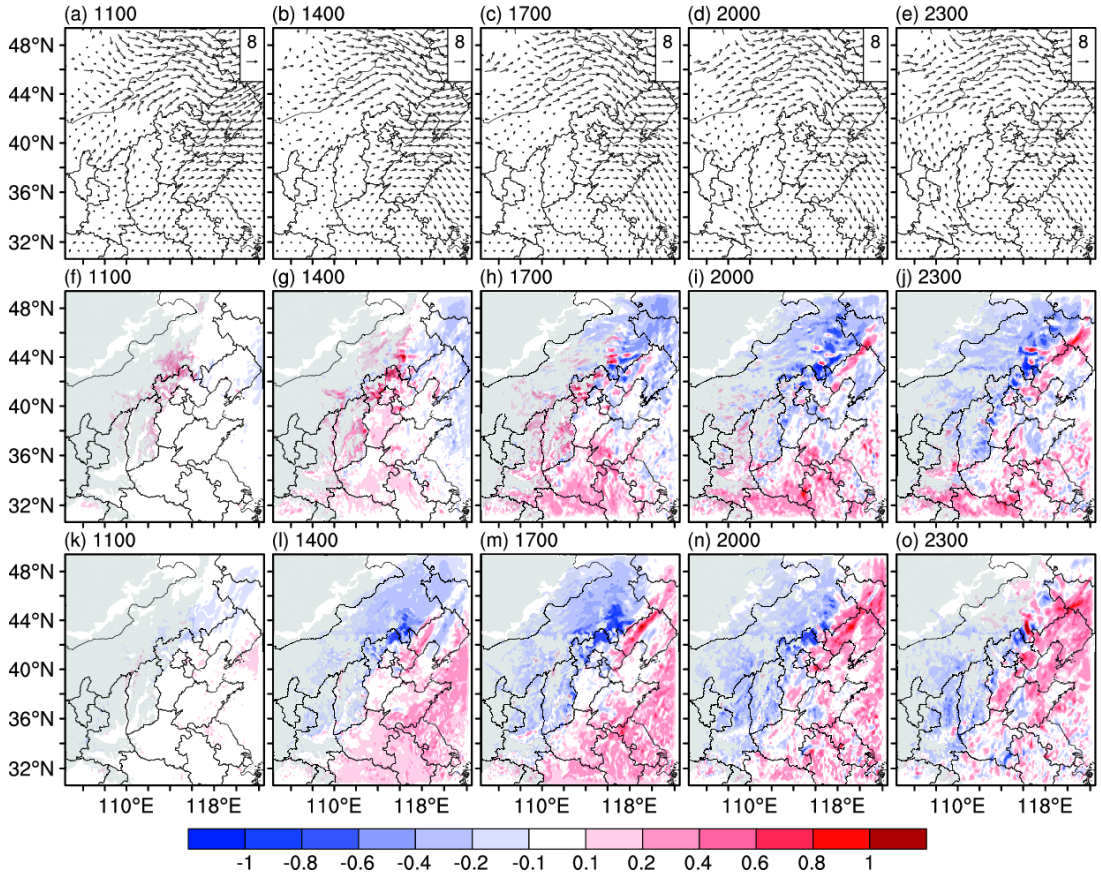

936

937 Figure 19. The wind at 850hPa (vector) at 1100, 1400, 1700, 2000 and 2300 LT in

938 NoAero averaged during 6th to 10th Dec. 2015. The difference of (f–j) U and (k–o) V

939 wind speed between Aero and NoAero (Aero minus NoAero). The grey areas denote

940 the areas of terrain height above 1000m.